MNRAS **000**, 1–18 (2020) Preprint 3 July 2020 Compiled using MNRAS LATEX style file v3.0

VALES VI: ISM enrichment in star-forming galaxies up to z~0.2 using ^{12}CO(1-0), ^{13}CO(1-0) and C^{18}O(1-0) line luminosity ratios

H. Méndez-Hernández, [1]★ E. Ibar,[1] K. K. Knudsen, [2] P. Cassata, [3,4] M. Aravena, [5] M. J. Michałowski, [6] Zhi-Yu Zhang, [7] M. A. Lara-López, [8] R. J. Ivison, [19] P. van der Werf, [10] V. Villanueva, [11] R. Herrera-Camus, [12] T. M. Hughes [13,1,14,15]

[1] *Insituto de Física y Astronomía, Universidad de Valparaíso, Avda. Gran Bretaña 1111, 2340000 Valparaíso, Chile*
[2] *Department of Space, Earth and Environment, Chalmers University of Technology, Onsala Space Observatory, SE-439 92 Onsala Sweden.*
[3] *Dipartimento di Fisica e Astronomia Galileo Galilei, Università degli Studi di Padova Vicolo delL'Osservatorio 3, 35122 Padova Italy*
[4] *INAF Osservatorio Astronomico di Padova, vicolo dell'Osservatorio 5, I-35122 Padova, Italy*
[5] *Núcleo de Astronomía, Facultad de Ingeniería y Ciencias, Universidad Diego Portales, Av. Ejército 441, Santiago, Chile*
[6] *Astronomical Observatory Institute, Faculty of Physics, Adam Mickiewicz University, ul. Słoneczna 36, 60-286 Poznań, Poland*
[7] *School of Astronomy and Space Science, Nanjing University, Nanjing 210093, China Key Laboratory of Modern Astronomy and Astrophysics (Nanjing University), Ministry of Education, Nanjing 210093, China*
[8] *DARK, Niels Bohr Institute, University of Copenhagen, Lyngbyvej 2, Copenhagen DK-2100, Denmark*
[9] *European Southern Observatory, Alonso de Córdova, 3107, Vitacura, Santiago 763-0355, Chile*
[10] *Leiden Observatory, Leiden University, P.O. Box 9513, NL-2300 RA Leiden, The Netherlands*
[11] *Department of Astronomy, University of Maryland, College Park, MD 20742, USA*
[12] *Astronomy Department, Universidad de Concepción, Barrio Universitario, Concepción, Chile*
[13] *Chinese Academy of Sciences South America Center for Astronomy, China-Chile Joint Center for Astronomy, Camino El Observatorio #1515, Las Condes, Santiago, Chile*
[14] *CAS Key Laboratory for Research in Galaxies and Cosmology, Department of Astronomy, University of Science and Technology of China, Hefei 230026, China*
[15] *School of Astronomy and Space Science, University of Science and Technology of China, Hefei 230026, China*

Accepted 2020 June 29. Received 2020 June 01; in original form 2019 December 04

ABSTRACT

We present Atacama Large Millimeter/sub-millimeter Array (ALMA) observations towards 27 low-redshift ($0.02 < z < 0.2$) star-forming galaxies taken from the Valparaíso ALMA/APEX Line Emission Survey (VALES). We perform stacking analyses of the ^{12}CO$(1-0)$, ^{13}CO$(1-0)$ and C^{18}O$(1-0)$ emission lines to explore the $L'(^{12}\mathrm{CO}(1-0))/L'(^{13}\mathrm{CO}(1-0)))$ (hereafter $L'(^{12}\mathrm{CO})/L'(^{13}\mathrm{CO})$) and $L'(^{13}\mathrm{CO}(1-0))/L'(\mathrm{C}^{18}\mathrm{O}(1-0))$ (hereafter $L'(^{13}\mathrm{CO})/L'(\mathrm{C}^{18}\mathrm{O})$ line luminosity ratio dependence as a function of different global galaxy parameters related to the star formation activity. The sample has far-IR luminosities $10^{10.1-11.9}\,\mathrm{L}_{\odot}$ and stellar masses of $10^{9.8-10.9}\mathrm{M}_{\odot}$ corresponding to typical star-forming and starburst galaxies at these redshifts. On average we find a $L'(^{12}\mathrm{CO})/L'(^{13}\mathrm{CO})$ line luminosity ratio value of 16.1±2.5. Galaxies with evidences of possible merging activity tend to show higher $L'(^{12}\mathrm{CO})/L'(^{13}\mathrm{CO})$ ratios by a factor of two, while variations of this order are also found in galaxy samples with higher star formation rates or star formation efficiencies. We also find an average $L'(^{13}\mathrm{CO})/L'(\mathrm{C}^{18}\mathrm{O})$ line luminosity ratio of 2.5±0.6, which is in good agreement with those previously reported for starburst galaxies. We find that galaxy samples with high L_{IR}, SFR and SFE show low $L'(^{13}\mathrm{CO})/L'(\mathrm{C}^{18}\mathrm{O})$ line luminosity ratios with high $L'(^{12}\mathrm{CO})/L'(^{13}\mathrm{CO})$ line luminosity ratios, suggesting that these trends are produced by selective enrichment of massive stars in young starbursts.

Key words: methods: statistical. techniques: interferometric. galaxies: star formation. galaxies: ISM.

★ E-mail: hugo.mendez@postgrado.uv.cl

1 INTRODUCTION

Stars are mostly formed within Giant Molecular Clouds (GMCs), cold dense regions of the interstellar medium (ISM), which are characterized by high densities ($n_{H_2} > 10^4$ cm^{-3}; Gao & Solomon 2004; Bergin & Tafalla 2007) and low temperatures (10–20 K; Evans 1999) that favour the formation of stars. In these regions, the most abundant molecule is molecular hydrogen, H_2, however its lack of a permanent electric dipole makes it difficult to observe in emission. After H_2, the next most abundant molecule is carbon monoxide, $^{12}C^{16}O$ (hereafter CO), which easily emits photons from low level rotational transitions in similar ISM conditions as those in which the H_2 molecule resides. Therefore, the CO emission from low-J rotational transitions have become the workhorse tracer of the H_2 gas mass in the local Universe and beyond (Bolatto et al. 2013).

Since the CO emission is mostly optically thick within GMCs, optically thin CO isotopologues are usually used to look deeper into the densest regions of GMCs. Since ^{12}C, ^{16}O and their isotopes, ^{13}C and ^{18}O, are mainly products of primary and secondary stellar nucleosynthesis processes, they are powerful tracers of the evolutionary state of a galaxy, and represent excellent tools to characterize the physical conditions and the chemical processes of the ISM (Wilson & Rood 1994; Milam et al. 2005; Romano et al. 2017). Narayanan & Krumholz (2014) showed that along side gas density and temperature, the optical depth from *low*-J CO lines is well correlated with the star formation rate surface density of GMCs. Moreover, it is possible to trace different stellar nucleosynthesis scenarios, by comparing ^{12}CO, ^{13}CO and $C^{18}O$ abundance variations. For example, Henkel & Mauersberger (1993) showed that dense regions that recently experienced a star formation event are expected to have higher abundances of $C^{18}O$ and ^{12}CO compared to ^{13}CO. The $^{12}C/^{13}C$ abundance ratio reflects the relative degree of primary to secondary nucleosynthesis processing, while the $^{18}O/^{16}O$ abundance ratio traces differences in the Initial Mass Function (IMF) (Milam et al. 2005; Romano et al. 2017). In practice albeit the optical depth effects, we could assume that the $^{12}C/^{13}C$ and $^{18}O/^{16}O$ abundance ratios can be traced by the molecular $I(^{12}CO)/I(^{13}CO)$ and $I(^{13}CO)/I(C^{18}O)$ line intensity ratios respectively

After the first detection of ^{12}CO and its isotopologues in the Milky Way (Wilson et al. 1970; Penzias et al. 1971), several works have repeated their detection in nearby galaxies (Rickard et al. 1975; Encrenaz et al. 1979; Rickard, & Blitz 1985; Young, & Sanders 1986). More recently, several works have proven successfully the usage of $I(^{12}CO)/I(^{13}CO)$ and $I(^{13}CO)/I(C^{18}O)$ line ratio in nearby galaxies (Sliwa et al. 2017; Jiménez-Donaire et al. 2017; Cormier et al. 2018; Sliwa et al. 2017; Brown & Wilson 2019), and lensed high-redshift galaxies (Henkel et al. 2010; Danielson et al. 2013; Spilker et al. 2014; Zhang et al. 2018).

An environmental dependence for $^{12}C/^{13}C$ has been shown by Alatalo et al. (2015), who found that 17 Early Type Galaxies (ETG) located in the Virgo cluster and groups, showed a line intensity ratio about two times lower than field galaxies. They proposed three different scenarios in which the observed variations could be explained: an extra low-mass stellar enrichment taking place in Virgo cluster galaxies, an increased mid-plane pressure effects of the intracluster medium (ICM) or the survival of only the densest clumps of molecular clouds as galaxies enter the ICM. Additionally, Davis (2014) showed a systematic dependence of the $I(^{12}CO)/I(^{13}CO)$ line intensity ratio on the star formation rate surface density (Σ_{SFR}) and the molecular gas surface density (Σ_{H_2}) using a sample of nearby starburst and early-type galaxies. They suggest that the observed correlations are caused by the combined action of massive stars heating and/or inducing turbulence in the gas phase on those galaxies with higher Σ_{SFR}.

Recent works have reported $I(^{13}CO)/I(C^{18}O)$ line intensity ratios for different galaxy types. Danielson et al. (2013) showed a low $I(^{13}CO)/I(C^{18}O)$ line intensity ratio (~1) in a high redshift lensed galaxy suggesting the presence of a significant fraction of high-mass stars. Sliwa et al. (2017) reported a simultaneous high $I(^{12}CO)/I(^{13}CO)$ ($\gg$60) intensity ratio with a low $I(^{13}CO)/I(C^{18}O)$ ($\lesssim$ 1) intensity ratio consistent with an ISM enrichment by the presence of a young starburst, a top-heavy IMF or their combined action. Jiménez-Donaire et al. (2017) presented a $I(^{13}CO)/I(C^{18}O)$ line intensity ratio dependency with Σ_{SFR} and galactocentric distance in nine nearby spiral galaxies due to the selective enrichment of the ISM by massive stars. More recently, Zhang et al. (2018) showed high $I(^{12}CO)/I(^{13}CO)$ line intensity ratios with a simultaneous low $I(^{13}CO)/I(C^{18}O)$ line intensity ratios in four gravitationally lensed sub-millimetre galaxies (SMGs) at z ~2-3, and claimed this to be caused by a change of the IMF where there is a higher number of massive stars in high-z starburst galaxies than in typical galaxies.

For galaxies beyond the Local Universe, the observation of faint emission lines as ^{13}CO or $C^{18}O$ is usually challenging. The abundances of ^{13}CO and $C^{18}O$ are typically 50 and 500 times lower than ^{12}CO (Jiménez-Donaire et al. 2017) and their flux density ratios usually range between 20 to 100 for I(^{12}CO)/I(^{13}CO) and between 20-140 for I(^{12}CO)/I(C^{18}O) (Aalto, et al. 1991; Casoli et al. 1992b; König et al. 2016; Sliwa et al. 2017). For individual detections in nearby local ULIRGs, ^{13}CO and $C^{18}O$ observations need to be at least four times deeper than ^{12}CO observations to yield line detections (Sliwa et al. 2017; Brown & Wilson 2019). In this work, we propose an alternative way to overcome sensitivity limitations by stacking the signals of the $^{12}CO(1-0)$, $^{13}CO(1-0)$ and $C^{18}O(1-0)$ lines ($\nu_{^{12}CO(1-0)}$ = 115.271 GHz, $\nu_{^{13}CO(1-0)}$ = 110.201 GHz, and $\nu_{C^{18}O(1-0)}$ = 109.782 GHz rest-frame frequencies, respectively) from individual star-forming galaxies to produce a statistically robust study for the content of these isotopologues up to z = 0.2.

This paper is structured as follows. In Section 2, we present the Atacama Large Millimetre/sub-millimetre Array (ALMA) data used in this work. Section 3 details the way we modelled the stacked ^{12}CO, ^{13}CO and $C^{18}O$ fluxes as well as their errors. Section 4 presents the $^{12}CO(1-0)/^{13}CO(1-0)$ and $^{13}CO(1-0)/C^{18}O(1-0)$ (hereafter $L'(^{12}CO)/L'(^{13}CO)$ and $L'(^{13}CO)/L'(C^{18}O)$) line luminosity ratio measurements and their dependence as a function of global galaxy parameters, while Section 5 presents the discussion. Finally, our conclusions are shown in Section 6. Throughout this work, we assume a ΛCDM cosmology adopting the values

$H_0 = 70\,km\,s^{-1}\,Mpc^{-1}$, $\Omega_M = 0.3$ and $\Omega_\Lambda = 0.7$ for the calculation of luminosity distances and physical scales.

2 DATA

2.1 Sample

In this work, we present ^{13}CO(1-0) and C^{18}O(1-0) line measurements for 27 and 24 galaxies, respectively, which were previously detected by *Herschel* in [C II] (Ibar et al. 2015) and with ALMA in ^{12}CO (Villanueva et al. 2017). The sample is part of the Valparaíso ALMA/APEX Line Emission Survey (VALES; Villanueva et al. 2017; Cheng et al. 2018) designed to characterize the CO emission line of low-J transitions from typical star-forming and starburst galaxies up to z = 0.35. The parent population comes from dusty galaxies taken from the equatorial fields of the *Herschel* Astrophysical Terahertz Large Area Survey (*H*-ATLAS; Eales et al. 2010.) Galaxies were selected using a spectroscopic redshift at $0.02 < z < 0.2$, and a *Herschel* detection near the peak of the spectral energy distribution (SED) of a normal star-forming galaxy ($S_{160\mu m} > 150\mu$Jy). All galaxies have an unambiguous optical counterpart in the Sloan Digital Sky Survey (SDSS; Adelman-McCarthy, et al. 2008), have high-quality spectra from the Galaxy and Mass Assembly survey (GAMA [1]; Liske et al. 2015; Driver et al. 2016 $z_{QUAL} \geq 3$), and show a Petrosian SDSS radii smaller than 15″ (see Ibar et al. 2015 for more details).

2.2 ALMA ^{13}CO(1 − 0) and C^{18}O(1 − 0) observations

Observations with ALMA in band-3 were performed as part of project 2013.1.00530.S (P.I. E. Ibar), targeting the redshifted ^{12}CO(1 − 0), ^{13}CO(1 − 0) and C^{18}O(1 − 0) emission lines for 27 VALES galaxies. The ^{12}CO(1 − 0) observations reached a root mean square (rms) of 2 mJy beam^{-1} at a spectral resolution of 30 km s^{-1} and are presented in Villanueva et al. (2017). The simultaneous ^{13}CO(1 − 0) and C^{18}O(1 − 0) observations were taken between 23 and 25 January 2015, in compact configuration (maximum baseline of ∼300 m) with precipitable water vapour (PWV) conditions in the range ∼4–6 mm. The observational strategy consisted of grouping sources in terms of redshift, such that we could observe all 27 galaxies using just three spectral setups (each one using four spectral windows to cover 7.5 GHz of bandwidth). The grouped sources are shown in Table 1, including the different executions performed by ALMA to reach the requested sensitivity. Unfortunately, the spectral setup missed C^{18}O(1−0) coverage in three galaxies.

Data reduction and imaging were performed using the same procedure as in Villanueva et al. (2017), where we developed a common pipeline within the Common Astronomy Software Applications (CASA version 4.4.0) to process all of the science goals. Each source was imaged with the TCLEAN task using a natu- ral weighting. This yielded a restoring beam between 3" and 4", nevertheless for the purposes of this work, we fixed the restoring beam to a common value, at 4.″5, for all sources. The ^{13}CO(1−0) and C^{18}O(1−0) observations reached rms noise of 0.9 mJy beam^{-1} at 30 km s^{-1} channel width (∼ 2× deeper than ^{12}CO observations). We note that ∼110 GHz continuum emission is undetected at 5σ significance in all sources down to a rms noise of 4μJy beam^{-1}.

[1] http://www.gama-survey.org/

3 ANALYSIS

Out of the 27 galaxies, 26 have been previously spectrally detected at > 5σ significance (signal-to-noise ratio: SNR) in ^{12}CO(1 − 0) (Villanueva et al. 2017). The ^{13}CO line was visually inspected for any individual detection. There were no confident ^{13}CO(1 − 0) emission lines from individual spectra for any of the 27 galaxies. Nevertheless, using the information of the ^{12}CO line widths as priors, we created moment-0 maps by collapsing the cube around ±1× FWHM$_{^{12}CO}$ of the expected ^{13}CO frequencies. In the collapsed images we identify 7 galaxies with SNR > 5. The remaining 21 galaxies have not been detected above a 5σ significance in their moment zero maps. Table 2 shows the SNRs, velocity integrated line flux densities and luminosities of these individual ^{13}CO detections. With respect to the C^{18}O emission line, we do not identify any detection in the spectra nor in the individual moment-0 maps using the same approach mentioned above.

Different techniques have been proposed to detect the emission of faint emission lines, falling below the detection limits. For example Loomis et al. (2018) proposed a matched filtering method that uses a previously identified high signal-to-noise emission line as a kernel for filtering the *uv* signal and thereby facilitate the detection of any contiguous faint emission line. Similarly, Yen et al. (2016) proposed an image-plane line detection technique tailored to boost the SNR of faint emission lines in keplerian disks. An independent approach has been the development of stacking techniques. This has been successful to detect the combined signal of faint emission coming from multiple objects of the same population over the electromagnetic spectrum, including the X-ray (Bartelmann & White 2003; Rodighiero et al. 2015; Yang et al. 2018), UV (Berry et al. 2012; Rigby et al. 2018), infrared (Dole, et al. 2006; Duivenvoorden et al. 2020), submm (Webb et al. 2003; Knudsen et al. 2005; Ibar et al. 2013; Millard et al. 2020), and radio (Miller et al. 2013; Bera et al. 2018; Perger et al. 2019) regimes. Moreover, stacking techniques have proven to be a robust method for line and continuum detections of high redshift galaxies (Scoville et al. 2007; Lehmer et al. 2007; Schinnerer et al. 2007; Miller et al. 2008). In order to compute stacked line ratios, in this study we explore three different techniques: two of them in the image plane: i) stacking all the moment-0 maps, ii) stacking all the frequency channels of all sources following a channel by channel basis, and additionally by iii) stacking the individual *uv*-plane average signals.

3.1 Image stacking

3.1.1 2D-moment-0 stacking

Based on the previously detected ^{12}CO line widths and intensity peaks, we collapsed the datasets to create moment-0 maps. For this, we measure ^{12}CO line widths using 20 km s^{-1} channel for all galaxies. Using the IMMOMENTS CASA task,

Table 1. New ALMA ^{13}CO(1 – 0) and C^{18}O(1 – 0) observations (Project ID: 2013.1.00530.S) presented in this work. 'PWV' is the average precipitable water vapour estimate for the observations. All data were taken using 32 12-m ALMA antennas. One observation taken on 24 January 2015 failed to run through the pipeline due to unknown reasons, so we have arbitrarily removed it from this work. Note that ^{12}CO(1 – 0) observations can be found in Villanueva et al. (2017).

Target names HATLAS	Observation Date	Flux Calibrator	Bandpass Calibrator	Phase Calibrator	PWV [mm]
J085340.7+013348, J085405.9+011130 J085356.4+001255, J083601.5+002617	2015 January 24 (1/3)	Ganymede	J1058+0133	J0909+0121	5.9
J085112.9+010342, J090949.6+014847 J085450.2+021208, J091205.8+002655	2015 January 24 (2/3)				5.2
J085346.4+001252, J084428.4+020350 J090005.0+000446, J090532.6+020222	~~2015 January 24 (3/3)~~				4.5
J085111.4+013006, J083745.1-005141, J085828.6+003813, J085233.9+013422	2015 January 25				4.5
J084350.8+005534, J083831.8+000044 J084305.1+010855 J084907.1-005138	2015 January 23 (1/2)	J0750+125	J0909+0121	J0901-0037	3.8
J084217.9+021223 J084139.6+015346 J085748.0+004641, J084428.4+020657	2015 January 23 (2/2)				3.9
J090750.0+010141, J085836.0+013149 J084630.9+005055	2015 January 23	J0854+201	J0750+1231	J0901-0121	3.8

Table 2. ^{13}CO(1–0) detections from collapsed spectral images using ±FWHM ^{12}CO km s^{-1} line width around ^{13}CO(1–0) expected frequencies. (col 1) ID taken from Villanueva et al. (2017), (col 2) observed signal-to-noise ratio in moment 0maps, (col 3) velocity integrated line flux densities with error measurements, (col 4) ^{13}CO(1 – 0) luminosity with error measurements.

ID HATLAS	SNR$_{^{13}CO}$	S$_{^{13}CO}\Delta$v mJy km s^{-1}	$L'_{^{13}CO}$ K km s^{-1}pc^2
J090949.6+014847	5.6	490 ± 90	68.0 ± 12.1
J085346.4+001252	5.7	225 ± 40	2.9 ± 0.5
J084139.6+015346	6.1	206 ± 33	5.4 ± 0.9
J084350.8+005534	6.2	458 ± 73	11.9 ± 2.0
J083831.8+000044	6.4	147 ± 22	4.3 ± 0.7
J085748.0+004641	5.9	343 ± 58	8.9 ± 1.5
J090633.6+001526	7.0	710 ± 100	9.6 ± 1.4

we collapse each galaxy cube to create moment-0 maps for all ^{12}CO, ^{13}CO and C^{18}O datasets, around (±1× FWHM$_{^{12}CO}$) the ^{12}CO, ^{13}CO and C^{18}O expected frequencies. We visually inspected all of the 27 collapsed ^{12}CO images to correct for any possible spatial offsets with respect to the intensity peak. Such offsets exist; optical and submm observations trace the stellar and the molecular gas content of galaxies respectively, and thus the location of the peaks do not necessarily match. Given that the reference coordinates of our ALMA observations were obtained from optical images, we apply astrometric corrections to our ^{12}CO intensity maps, in order to correct any discrepancy between optical and ^{12}CO images. These corrections are on average of the order of ~ 1.″4 in random directions (smaller than the synthesized beam of 4.″5). Finally, using a stacking code that we developed, these images were stacked to obtain final collapsed signals reaching rms values of 108 mJy beam^{-1} km s^{-1} for the ^{12}CO line and 18 mJy beam^{-1} km s^{-1} for the ^{13}CO and C^{18}O emission lines. We note that these stacked values are ~ 5 times deeper than individual moment-0 images.

To extract velocity integrated line flux densities from the stacked signals, we create 30" × 30" stamps and model the sources with a 2D Gaussian profile, assuming that the stacked signals are point-like with a FWHM of 4.″5.

3.1.2 3D-image stacking

In this approach, for processing the datacubes, we consider a common spectral channel width for ^{12}CO, ^{13}CO and C^{18}O emission lines. To determine the best common spectral channel width to use, we kept in mind the idea of optimizing the SNR of the final stacked data cubes detections of both lines. For this, datacubes for all of the 27 galaxies were created using CASA task TCLEAN assuming different velocity bin widths: [20, 40, 50, 80, 100, 125, 160, 200, 250, 400, 500, 800] km s^{-1}. After this, we obtained a 3D stacked cube by combining the individual galaxy cubes following a channel by channel and pixel by pixel basis. We then obtained the SNR by measuring the peak at the central image pixel and central velocity channel (0km s^{-1}). We measured the noise in the image excluding the central region. Peak flux densities were recorded for both the mean and median stacked cubes with different velocity width bins and for ^{12}CO, ^{13}CO and C^{18}O data sets. Figure 1 shows this central channel SNR as a function of channel velocity width. We find that the ^{12}CO signal maximizes at channel width of 200 km s^{-1} for both the median (SNR~105.7) and mean (SNR~96.6). The stacked ^{13}CO line maximizes at 125km s^{-1} (SNR~8.0) and 500km s^{-1} (SNR~10.1) for the median and mean respectively. Finally, the C^{18}O line maximizes at 125km s^{-1} for both the median (SNR~4.7) and the mean (SNR~5.5) stacks. Based on these results we decided to use a common spectral channel width of 125 km s^{-1} for ^{12}CO, ^{13}CO and C^{18}O to image all data cubes in order to optimize the signal-to-noise ratio in the final stacked images. We note that the same astrometric offsets used for moment-0 stacking, and

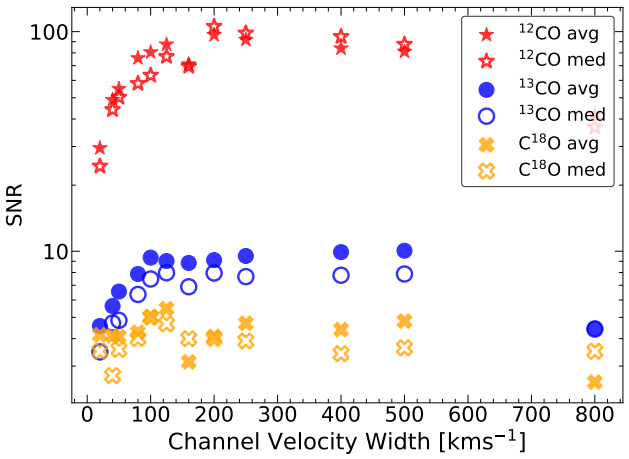

Figure 1. Stacked signal-to-noise ratios (SNRs) obtained from ^{12}CO (stars), ^{13}CO (circles) and C^{18}O (crosses) using different velocity channel widths, from 20 km s^{-1} to 800 km s^{-1}. Filled symbols correspond to average SNR values while empty symbols correspond to median SNR values. These measurements are used to identify the best spectral channel width for 3D stacking (see § 3.1.2).

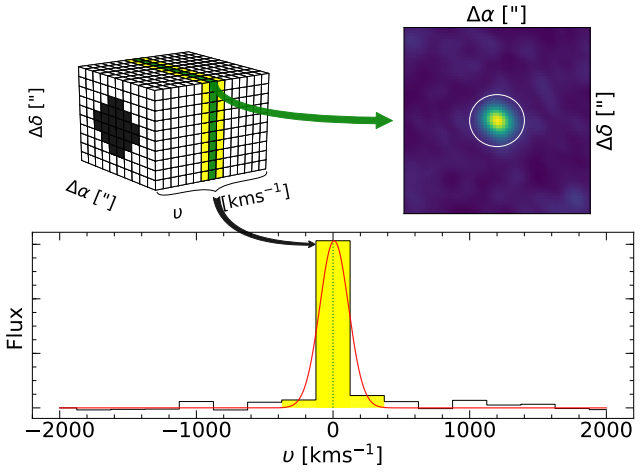

Figure 2. Velocity integrated flux density measurements on a 3D stacked data cube. Upper left panel: 3D stacked image cube showing the central channel (green) at which the peak of the line is located, the channels covered by the fit FWHM$_f$ line width highlighted in yellow and the 15″ radius aperture (black) used to generate the spectral line profile shown below. The bottom panel shows the spectral line profile (solid black line) and shows the 1D gaussian fit (red line) to obtain the stacked velocity line width FWHM$_f$ highlighted in yellow. The upper right panel shows the central channel where a 2D Gaussian profile is fit (white) to obtain the amplitude of source. Both line width and amplitude are used to compute the velocity integrated line flux densities.

described in Section 3.1.1 have been applied here, whilst velocity offsets based on the peak observed in ^{12}CO are applied to all of the independent cubes in order to re-centre the signal. These offsets originate from small differences between the optical and submm redshifts which trace different phases of the ISM.

Using a common channel width of 125 km s^{-1}, a spectral coverage of ±2000km s^{-1}, and a restoring beam with a FWHM of 4.″5, we created the individual datacubes which are then stacked to get a cube containing the average ^{12}CO, ^{13}CO and C^{18}O signals. In order to measure velocity integrated line flux densities, we first created spectral line profiles using a fixed aperture of 15″ radius ($\gtrsim$3×synthesized beam), centred at the source position. Thereby, we fitted a 1D Gaussian profile to obtain the global stacked velocity line width FWHM$_f$ (see Fig. 2 lower panel). Hence, we took the central channel (0km s^{-1}, where the peak in the spectral line profile is located) to fit a 2D Gaussian profile assuming that the signal is point-like (see Fig. 2 upper right panel). Finally, the amplitude of the 2D Gaussian fit together with the line width, is used to calculate velocity integrated line flux densities.

3.1.3 Systematic Errors

In order to compute the systematic errors for our stacked velocity integrated line flux density measurements, we ran Monte-Carlo simulations using data cubes with the same physical scales (pixel size, synthesised beam, primary beam) as those covered by the ALMA Band-3 observations.

We model each source as point-like (spatially) using a 2D circular Gaussian profile and spectrally by a 1D Gaussian profile centered at 0 km s^{-1}. We simulate a spectral coverage of ±2000 km s^{-1}. These sources are added to a random, normally-distributed background noise that has been convolved to the scale of the synthesised beam.

To simulate the stacking, we take 27 data cubes with sources at fixed signal-to-noise ratios (<SNR$_{\rm in}$>) and fixed velocity line widths. We stacked them and compute the velocity integrated line flux densities as described in Sections 3.1.1 and 3.1.2. We repeat this process 1000 times, where amplitudes and velocity widths are simulated to take fixed values between 0 and 100 times the rms and line FWHMs between 50 and 500 km s^{-1}, respectively. The extracted velocity integrated line flux densities ($S_{\rm out}$) are measured and compared to the input values. Figure 3 shows the $<S_{\rm in}>/S_{\rm out}$ ratio of 1000 simulated stacked data cubes for both, 2D-moment-0 (open stars) and 3D-image (open circles) stacking methods. The average binned $\overline{<S_{\rm in}>/S_{\rm out}}$ ratios (filled symbols in Fig. 3) as a function of SNR$_{\rm out}$ of the composite stack images in the range between zero and 520 (= 100×$\sqrt{27}$). We note that the stacked images have SNR$_{\rm out}$ that are ~ $\sqrt{27}$ times larger than the average <SNR$_{\rm in}$> of the individual images given by Poisson factor gained by the stacking approach. For example, if the ^{13}CO stack has a measured SNR$_{\rm out}$ ~9, then this is produced by individual datacubes with an average <SNR$_{\rm in}$>~1.73. Figure 3 shows vertical lines indicating three different SNRs values ~6, ~13 and ~18 at which our 3D-stacks show systematic errors of 8%, 3% and 2% while 2D-moment-0 stacks show 5%, 3% and 1%. These results show how typically 2D-stacks show smaller systematic errors than 3D-stacks. These differences tend to become negligible at SNRs>15.

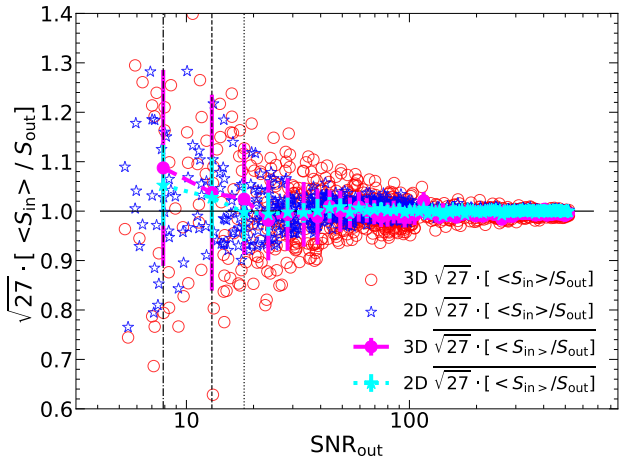

Figure 3. Simulated accuracy of the velocity integrated flux density measurements ($<S_{in}>/S_{out}$) after stacking 27 galaxies. Stacked detections with high SNR$_{out}$ have clearly better accuracy for the velocity integrated flux density measurements. $<S_{in}>$ refers to the average velocity integrated flux densities of the simulated sources used for the stacks, while S_{out} refers to the measured velocity integrated flux density on the composite stacked images. 3D stacks are shown as open circles, 2D moment-0 stacks are shown as open stars and filled symbols indicate the average $\overline{<S_{in}>/S_{out}}$ binned by SNR$_{out}$. Vertical lines indicate the location of our ^{12}CO, ^{13}CO and C^{18}O SNR$_{out}$ stacked detections at ~6 (dashed-dotted), ~13 (dashed) and ~18 (dotted) where 3D-image stacks show systematic errors of 8%, 3% and 2% while 2D-moment-0 stacks show 5%, 3% and 1% respectively.

3.2 *uv* stacking

Interferometric telescopes provide data that samples the brightness distribution of an observed source in Fourier space, where a point measurement per integration time is provided by a pair of antennas. The location of every point (visibility) in the Fourier space (*uv*-plane) is determined by the separation of a pair of antennas as they trace the track of the source in the Fourier space during integration. The imaging process considers a deconvolution which assumes interpolations made on the *uv*-plane that could lead to artifacts in the extracted images due to the intrinsic non-continuous sampling nature of interferometric datasets (Condon, & Ransom 2016). Interferometric stacking analyses are usually performed using these reconstructed images. Lindroos et al. (2015) developed *stacker* [2], a tool which directly stacks interferometric continuum datasets in the *uv*-plane providing typical signal-to-noise ratios which are 20% higher compared with continuum image stacking. *Stacker* was designed to perform the stacking analysis for continuum *uv*-data, therefore we mimic continuum maps as the average single channel maps of the ^{12}CO, ^{13}CO and C^{18}O emission lines intensity data of the galaxies. To create individual single channel maps we use the CASA task SPLIT to obtain an average *uv*-data of the channels around the ^{12}CO line observed frequency (±1× FWHM$_{^{12}CO}$). As described in Section 3.1.1 ^{12}CO line widths were measured using a 20km s^{-1} resolution, and these widths were also used to create the individual single channel maps for the ^{13}CO and C^{18}O datasets. Similarly to previous approaches, we note that we have applied the same astrometric offset corrections to generate the single channel *uv* maps. To measure velocity integrated line flux densities from the *uv* stacks, we create images using CASA task TCLEAN following a similar approach as the images used for 2D and 3D-image stacking procedures. Then as in 2D-stacks, we model the sources with a 2D Gaussian profile and measured the velocity integrated line flux densities from 30" × 30" stamps.

[2] https://www.oso.nordic-alma.se/software-tools.php

3.3 The differences between the stacking approaches

In this section we discuss the stacking approaches described above in order to decide the most suitable one for our work. As mentioned before, each method is based on different assumptions, therefore a direct comparison is not entirely trivial. For example, the images obtained from 2D-stacking are generated using CASA task IMMOMENTS which basically sums the intensities of the channels around ±1×FWHM$_{^{12}CO}$ for the ^{12}CO observed frequency, while the ^{13}CO and C^{18}O lines are blindly extracted at the expected frequencies using the derived ^{12}CO redshifts. The 3D approach concentrates mainly on highlighting the intensities from the central channel of data cubes, where the velocity peak of the flux density profile is located. The case for the stacks obtained from a *uv* approach are constructed starting from CASA task SPLIT which averages the *uv* intensities of the channels where the lines are located, these channels are exactly the same as those channels used to create the moment-0 maps for 2D-stacking.

In Fig. 4 we show 30"×30" image stacks and residuals after point-source extraction for the three methods explored in this work. All three different approaches result in similar velocity integrated line flux densities within the errors. However, we find that for a bright line like ^{12}CO *uv* stacks shows a SNR ~1.6× higher than that obtained from 2D stacking method (see Table 3). This result is similar to that found by Lindroos et al. (2015) who reported that continuum *uv* stacking signal-to-noise ratio was up to 20% higher than the continuum image stacking. Nevertheless, we find that for ^{12}CO 3D-image stacking shows to be the method with the highest SNR, being 2.5 and 1.6 times higher than 2D-moment-0 stacking and *uv* stacking SNRs respectively. On the other hand the 3D stacking method shows the lowest SNR for the faint lines like ^{13}CO, while the 2D-moment-0 and *uv* stacking methods show similar SNRs. We note that, all the stacking methods applied on C^{18}O emission line show similar SNRs. Even though *stacker* was specially designed to stack *uv* continuum datasets and it has been successfully applied for *uv* emission line stacking (Fujimoto et al. 2018, 2019; Fudamoto et al. 2020; Carvajal et al. 2020) using a similar procedure as described here, this is the first time that *uv* and image stacking methods for emission line observations are directly compared. Driven by the previously available ^{12}CO data presented in Villanueva et al. (2017), we decide to use the 2D (moment-0) approach to measure values, as this method yields the highest ^{13}CO stacked SNRs that are straightforward to interpret and simple to calculate

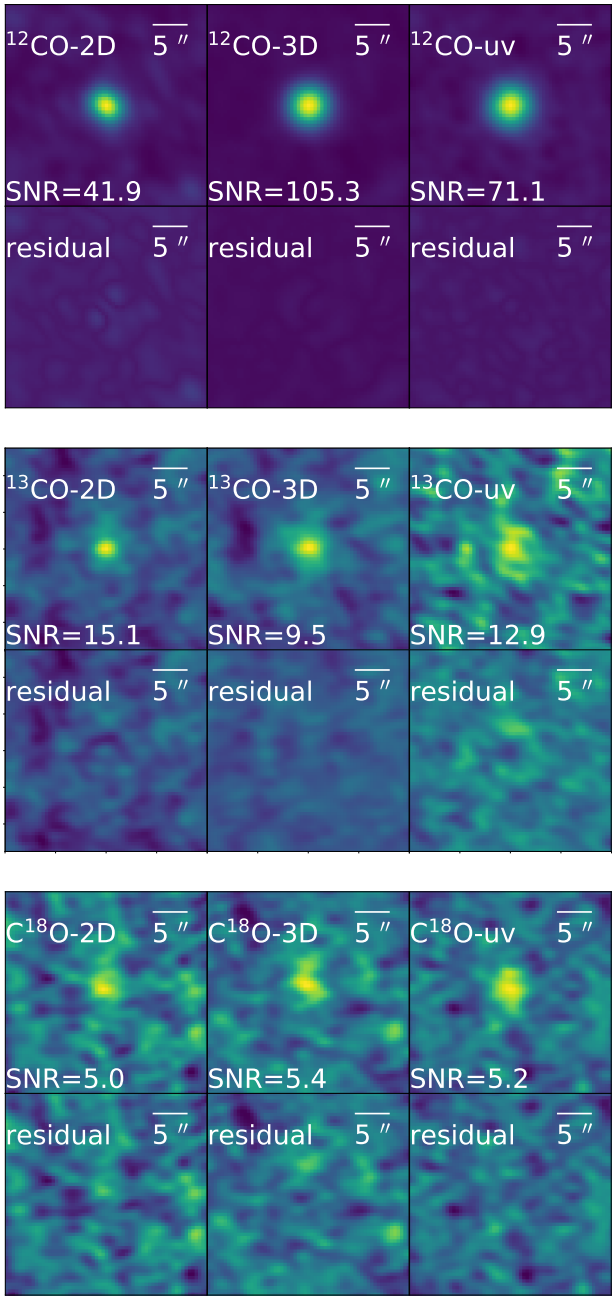

Figure 4. Final composite 30"×30" stamps stacks (top)and residuals (bottom) from the corresponding flux modelling (see Section 3) for ^{12}CO (upper panels), ^{13}CO (middle panels) and C^{18}O (lower panels) emission lines from 2D-moment-0 stack (left column), 3D-image stack (middle column) and *uv* stack (right column).

3.4 Luminosity measurements

We compute the ^{12}CO, ^{13}CO and C^{18}O luminosities using the velocity integrated line flux densities following (Solomon & Vanden Bout 2005):

$$L'_{\rm CO} = 3.25\times10^7 S\Delta v \nu_{\rm obs}^{-2} D_{\rm L}{}^2 (1+z)^{-3} \quad (1)$$

where $L'_{\rm CO}$ is measured in K km s^{-1} pc^2, $S\Delta$v is the velocity integrated line flux density in units of Jy km s^{-1}, $\nu_{\rm obs}$ is the observed frequency of the emission line in GHz, $D_{\rm L}$ is the luminosity distance in Mpc, and z is the redshift.

Considering the fact that we are analysing average properties from galaxies at different redshifts, special consideration should be taken to convert to intrinsic luminosities. To determine the dispersion of the stacked luminosity measurements we have used a Monte Carlo simulation considering that the error from the velocity integrated line flux density measurements is normally distributed, and at the same time assume a random sampling for the redshift distribution of the parent stacked sample. Repeating this simulation, we get a distribution of luminosities from which we can then infer the 1σ confidence intervals (CI) of our average luminosity measurements. Since each galaxy population has a different redshift distribution, their CIs are independent from one population to another. We note that the differences between intensity and luminosity ratio measurements are negligible. The luminosity ratio of any pair of lines (L'_1, L'_2) comes from converting their fluxes into luminosities following Equation 1. Given that the redshifts (z_1, z_2) for both lines are the same, the redshift and luminosity distance dependencies vanish leading to Equation 2.

$$\frac{L'_1}{L'_2} = \frac{S_1\Delta v_1 \nu_1^{-2} D_{\rm L_1}^{-2}(1+z_1)^{-3}}{S_2\Delta v_2 \nu_2^{2} D_{\rm L_2}^{2}(1+z_2)^{-3}} = \frac{I_1\nu_1^{-2}}{I_2\nu_2^{-2}} \quad (2)$$

In particular $L'(^{12}{\rm CO})/L'(^{13}{\rm CO}) = 0.91 \times I(^{12}{\rm CO})/I(^{13}{\rm CO})$ and $L'(^{13}{\rm CO})/L'({\rm C}^{18}{\rm O}) = 0.99 \times I(^{13}{\rm CO})/I({\rm C}^{18}{\rm O})$, which enable us to make direct comparisons between our results and different intensity and luminosity ratios available in the literature.

Table 3. Signal-to-noise Ratio (SNR) detection for ^{12}CO, ^{13}CO and C^{18}O stacked line emission, obtained from three different stacking methods explored in this work 1) 2D-moment-0 stacking, 2) 3D-image stacking and 3) *uv* stacking.

SNR	Moment-0	*uv*-stacking	3D-stacking
^{12}CO	41.9	71.1	105.3
^{13}CO	15.1	12.9	9.5
C^{18}O	5.0	5.2	5.4

4 RESULTS

4.1 The $L'(^{12}{\rm CO})/L'(^{13}{\rm CO})$ ratio

The VALES survey provides a wide range of global galaxy properties such as stellar masses, star formation rates, morphologies, luminosities etc. In this section, we present the measured $L'(^{12}{\rm CO})/L'(^{13}{\rm CO})$ luminosity ratios to search for possible dependencies on different global galaxy parameters.

4.1.1 Morphological and environmental dependence

A morphological and environmental dependence of the $I(^{12}{\rm CO})/I(^{13}{\rm CO})$ line intensity ratio has been reported by previous studies. While merger systems show a higher

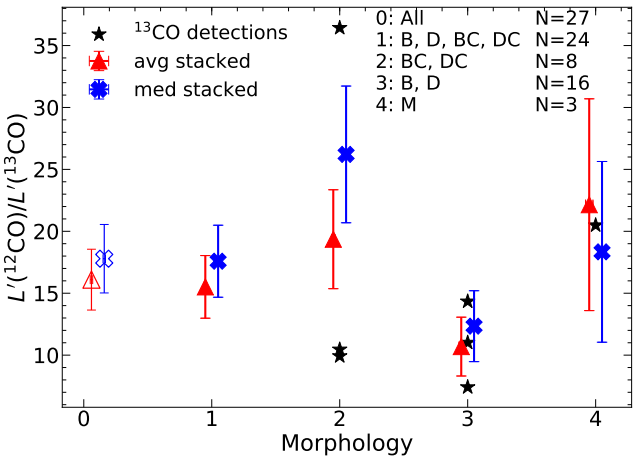

Figure 5. Average (red triangles) and median (blue crosses) stacked $L'(^{12}CO)/L'(^{13}CO)$ line luminosity ratio values as a function of optical morphological properties as presented in Villanueva et al. (2017): 0) all galaxies (n=27) open symbols, 1) all galaxies excluding mergers (B, D, BC, DC; n=24); 2) bulge and disc dominated galaxies with projected companions (BC, DC; n=8); 3) bulge and disc dominated galaxies without any companion (B, D; n=16); and 4) mergers (M; n=3). Error bars correspond to 1 σ confidence intervals for average ratios.

$I(^{12}CO)/I(^{13}CO)$ intensity ratio when compared with normal spiral galaxies (Casoli et al. 1992b; Taniguchi & Ohyama 1998; Taniguchi et al. 1999), galaxies in dense environments show a lower $I(^{12}CO)/I(^{13}CO)$ intensity ratio (Alatalo et al. 2015). Initially, we explore the morphological and environmental classification available for our sample, according to the most prominent morphological features: Bulge (B), Disc (D), Merger-Irregular (M), and (C) which denotes if the source has multiple projected neighbouring systems ("companions"), as based on a visual inspection presented by Villanueva et al. (2017) to multi-wavelength imaging from the GAMA survey.

We split our sample into 5 different subsets: 0) all galaxies; (n=27; open symbols), 1) all galaxies excluding clear mergers (B, D, BC, DC; n=24); 2) bulge and disc dominated galaxies with projected companions (BC, DC; n=8); 3) bulge and disc dominated galaxies without any companion (B, D; n=16); and 4) mergers (M; n=3) (see Figure 5).

In Table 4 we present the measured average $L'(^{12}CO)/L'(^{13}CO)$ line luminosity ratio and average <SFR>, <SFE>, and $<L_{IR}>$ values for the five different morphological galaxy populations explored in this work. Using all of the 27 galaxies, we find an average $L'(^{12}CO)/L'(^{13}CO)$ line luminosity ratio of 16.1±2.5. This value is in agreement with the values for mergers (12±3) and interacting early type galaxies (ETGs) (15±5) reported by Alatalo et al. (2015), and to the ratio of nearby spirals, starburst and ETGs (excluding those belonging to the Virgo Cluster used by Alatalo et al. 2015) reported by Davis (2014) (12±1.0). Mergers and galaxies with a visible companion tend to show higher $L'(^{12}CO)/L'(^{13}CO)$ line luminosity ratios. In particular, mergers show the highest <SFR>, <SFE>, and $<L_{IR}>$ average values among the different morphological classifications, and also show a $L'(^{12}CO)/L'(^{13}CO)$ line luminosity ratio 2 times higher than that found in galaxies without a companion. These findings, however, are at low significance (mainly due to the low number statistics). Besides, these ratios are in good agreement with the ratios reported by Alatalo et al. (2015), who found that group galaxies present $L'(^{12}CO)/L'(^{13}CO)$ line luminosity ratios 2 times higher than field galaxies.

4.1.2 The star-formation activity

Villanueva et al. (2017) derived various global galaxy properties, including star formation rate (SFR), star formation efficiency (SFE), molecular gas surface density (Σ_{H_2}), star formation rate surface density (Σ_{SFR}), stellar mass ($M_\star$), gas depletion time (τ), and projected size (R_{FWHM}). The total IR luminosity was obtained as described in Ibar et al. (2015) by integrating the best-fitting SED between 8 and 1000 μm using photometry from IRAS, Wide-field Infrared Survey Explorer (WISE), and *Herschel*. The star formation rate was estimated following SFR ($M_\odot yr^{-1}$) = $10^{-10}\times L_{IR}$ assuming a Chabrier (2003) IMF. The molecular gas mass was computed using L'_{CO} and assuming an α_{CO} conversion factor dependent on the morphological classification (α_{CO} = 4.6 K km s^{-1} pc^2 for B and D dominated galaxies and α_{CO} = 0.8 K km s^{-1} pc^2 for mergers/interacting galaxies). The SFR and M_{H_2} surface densities were estimated by dividing the measured values by the area of a two-sided disc ($2\pi R^2_{FWHM}$), where R_{FWHM} is the deconvolved FWHM along the semimajor axis obtained through fitting elliptical gaussian profiles to the ^{12}CO (1–0) moment-0 maps using the CASA task IMFIT. We consider the CO emission to be spatially resolved if the fitted semimajor axis is at least $\sqrt{2}$ times larger than the semimajor axis of the synthesized beam. A more detailed discussion about the computations of these parameters can be found in Villanueva et al. (2017). With these in hand, we looked for possible dependencies of $L'(^{12}CO)/L'(^{13}CO)$ luminosity line ratio on these global galaxy properties by splitting our sample in two bins for each parameter. Figure 6 shows the redshift, L_{IR}, SFR, SFE, Σ_{SFR} and Σ_{H_2} distributions, split by low and high values. We find that the most significant trends for the $L'(^{12}CO)/L'(^{13}CO)$ ratios are with L_{IR}, SFR, and SFE (see Figures 7 and 8). Table 5 shows the average $L'(^{12}CO)/L'(^{13}CO)$ line luminosity ratios for low and high L_{IR}, SFR, SFE, Σ_{SFR} and Σ_{H_2} populations.

Figure 7 shows a trend of $L'(^{12}CO)/L'(^{13}CO)$ line luminosity ratio with L_{IR} similar to that shown by Taniguchi & Ohyama (1998) who used ^{12}CO and ^{13}CO line data taken from the literature for 61 nearby galaxies, including eight luminous starburst galaxies. They found a correlation between L_{FIR} and $L'(^{12}CO)/L'(^{13}CO)$ line ratio, where starburst galaxies with high infrared luminosities show higher ($L'(^{12}CO)/L'(^{13}CO) \geq 20$) line ratios compared with normal galaxies. They dismissed physical gas properties such as density, temperature, or velocity gradients as responsible for the observed high $L'(^{12}CO)/L'(^{13}CO)$ abundance ratio in starburst galaxies and conclude that the only possible mechanism behind the high ^{12}CO/^{13}CO abundance ratio in starburst galaxies is an underabundance of ^{13}CO with respect

Table 4. Average $L'(^{12}CO)/L'(^{13}CO)$ line luminosity ratio and average <SFR>, <SFE> and $<L_{IR}>$ values for different morphological classifications explored in this work (Villanueva et al. 2017; see § 4.1.1 for more details).

ID	Group	N	$L'(^{12}CO)/L'(^{13}CO)$	<SFR> $M_\odot yr^{-1}$	<SFE> Gyr^{-1}	$<\log[L_{IR}/L_\odot]>$
0	All	27	16.1 ± 2.5	14.9 ± 3.8	1.9 ± 0.5	10.9 ± 0.5
1	BC,DC,B,D	24	15.5 ± 2.5	12.7 ± 4.2	0.9 ± 0.1	10.8 ± 0.5
2	BC,DC	16	19.4 ± 4.0	17.6 ± 5.9	1.0 ± 0.1	11.0 ± 0.5
3	B,D	8	10.7 ± 2.4	3.4 ± 0.5	0.8 ± 0.1	10.5 ± 0.2
4	M	3	22.1 ± 8.6	34 ± 6.9	9.6 ± 0.8	11.5 ± 0.2

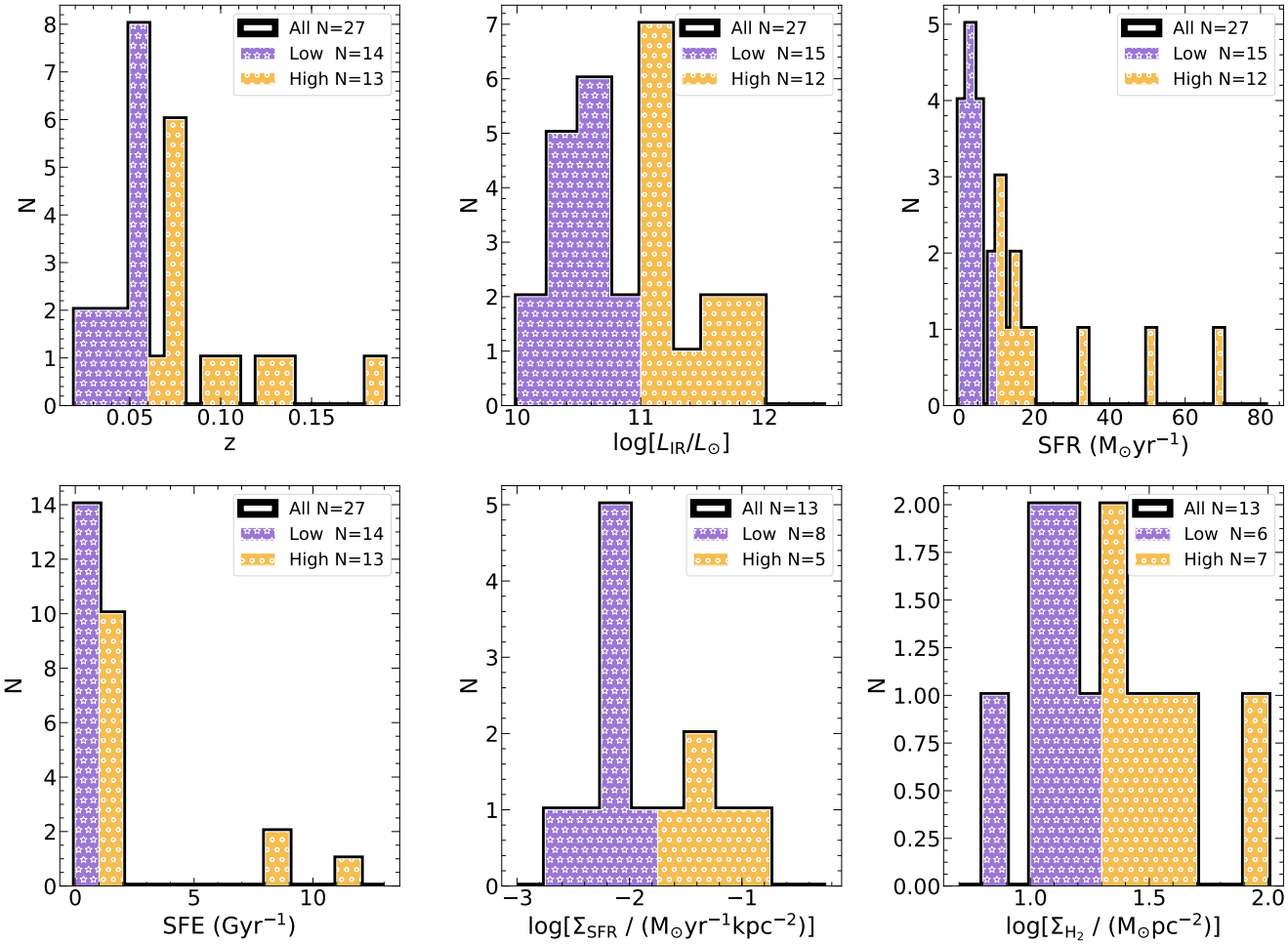

Figure 6. Redshift, L_{IR}, SFR, SFE, Σ_{SFR} and Σ_{H_2} distributions of the galaxies used in the ^{12}CO and ^{13}CO stacking analysis (solid black line), split by low (purple bars hatched with stars) and high (yellow bars hatched with circles) values.

to ^{12}CO. Our stacks (see Figure 7) show a trend in which the high L_{IR} sample falls in the starburst region, while the low L_{IR} sample shows an average $L'(^{12}CO)/L'(^{13}CO)$ line luminosity ratio similar to that found in normal galaxies.

To test the significance of the $L'(^{12}CO)/L'(^{13}CO)$-L_{IR} variations we applied a Student's t-test to determine the probability that the $L'(^{12}CO)/L'(^{13}CO)$ line luminosity ratio variations between the low and high L_{IR} populations are not statistically significant. A large p-value indicates that the differences between the two sample means are not statistically significant, while a small one suggests that the differences between the two sample means are significant. Based on this test we find that the differences in the $L'(^{12}CO)/L'(^{13}CO)$-L_{IR} variations are statistically significant (see Table 5). We then implemented a Spearman rank test to investigate a possible $L'(^{12}CO)/L'(^{13}CO)$-L_{IR} correlation, where p-values report the probability of the lack of correlation between the two samples. A large p-value indicates that there is no significant correlation, while a small one suggests a significant correlation. The Spearman rank test was computed considering six galaxies (excluding HATLASJ090949.6 identified as an outlier see Section

Table 5. Average $L'(^{12}CO)/L'(^{13}CO)$ line luminosity ratio for our sample of galaxies split by high and low L_{IR}, SFR, SFE, Σ_{SFR} and Σ_{H_2} values. Column 1: Parameter of interest; Column 2: Range explored; Column 3: Number of galaxies in the explored range; Column 4: Average value for parameter of interest; Column 5: The average stacked $L'(^{12}CO)/L'(^{13}CO)$ line luminosity ratio; Column 6 and 7: Student's t-test statistical reports (t, p) to asses the probability (p) that the null hypothesis ($L'(^{12}CO)/L'(^{13}CO)$ line luminosity ratio variations between the low and high SFR populations is not statistically significant), is true.

Parameter	Range	N	Average	$L'(^{12}CO)/L'(^{13}CO)$	t-test	
					t	p
1	2	3	4	5	6	7
$\log[L_{IR}/L_\odot]$	[10.1 - 10.9]	14	10.5 ± 0.1	13.8 ± 2.4	-3.9	0.0006
	[11.0 - 11.9]	13	11.3 ± 0.1	18.7 ± 3.9		
SFR ($M_\odot yr^{-1}$)	[1.8 - 9.5]	15	3.9 ± 0.6	13.3 ± 2.4	-4.3	0.0002
	[10.3 - 83.4]	12	28.6 ± 5.3	18.7 ± 3.8		
SFE (Gyr^{-1})	[0.4 - 0.9]	14	0.6 ± 0.1	12.9 ± 2.7	-4.7	7E-05
	[1 - 11.7]	13	3.3 ± 0.6	19.4 ± 4.2		
$\log[\Sigma_{SFR}$ / $(M_\odot yr^{-1} kpc^{-2})]$	[-2.6 - -1]	13	-1.8 ± 0.1	12.5 ± 2.4	-0.05	0.9
	[-2.6 - -2]	8	-2.2 ± 0.1	12.2 ± 3.1		
	[-2.1 - -1]	5	-1.3 ± 0.1	12.3 ± 3.5		
$\log[\Sigma_{H_2}$ / $(M_\odot pc^{-2})]$	[0.8 - 2.0]	13	1.3 ± 0.1	12.5 ± 2.5	-0.5	0.6
	[0.8 - 1.2]	6	1.0 ± 0.1	11.8 ± 3.2		
	[1.3 - 2.0]	7	1.6 ± 0.2	12.8 ± 3.5		

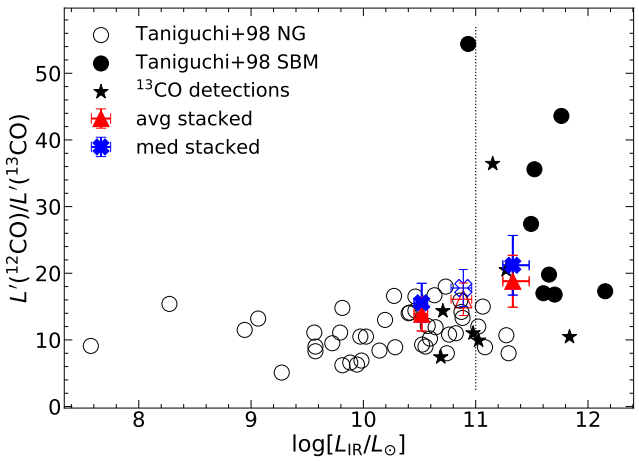

Figure 7. Average (red triangles) and median (blue crosses) stacked $L'(^{12}CO)/L'(^{13}CO)$ line luminosity ratio for low and high L_{IR} subsets (triangles). A dashed line indicates the boundary between low and high L_{IR} populations. As reference average and median line luminosity ratio considering all galaxies in open symbols are included. Error bars correspond to 1σ confidence intervals for average or median values based Monte-Carlo simulations. Individual ^{13}CO detections (stars) and $L'(^{12}CO)/L'(^{13}CO)$ line luminosity ratios of normal galaxies (NG open circles) and starburst mergers (SBM filled circles) scaled by a 1.75 factor to convert from far-IR to IR luminosities (see Appendix E from Herrera-Camus et al. 2015) from Taniguchi & Ohyama (1998)are also included.

4.1.3) with individual ^{13}CO detections, for which we could compute individual $L'(^{12}CO)/L'(^{13}CO)$ luminosity ratios. The Spearman rank test does not provide evidence (see Table 6 first row) supporting a significant correlation between $L'(^{12}CO)/L'(^{13}CO)$ and L_{IR}. This might be due to the reduced number (6) of galaxies with individual ^{13}CO detections covering a small range of L_{IR}. However, if we also consider starburst galaxies and normal galaxies covering a wider range of L_{FIR} as reported by Taniguchi & Ohyama (1998), we find (see Table 6 second row) evidence supporting a moderate $L'(^{12}CO)/L'(^{13}CO)$-L_{IR} correlation.

Table 6. Spearman correlation test statistic (ρ, p), to asses the null hypothesis (no significant correlation between $L'(^{12}CO)/L'(^{13}CO)$ and L_{IR}) being true, for 1) 6 galaxies with ^{13}CO individual detections for which we could compute individual $L'(^{12}CO)/L'(^{13}CO)$ luminosity ratios and 2) 6 galaxies with ^{13}CO individual detections plus 61 starburst and normal galaxies reported by Taniguchi & Ohyama (1998).

Sample	N	ρ	p
1) Galaxies with ^{13}CO detections	6	0.71	0.14
2) + Starburst and Normal galaxies	67	0.55	4E-6

Figure 8 (upper panels) shows $L'(^{12}CO)/L'(^{13}CO)$ line luminosity ratio trends with SFR and SFE. Considering that SFRs are derived from far-IR luminosities, an expected trend in SFR is also identified (see Fig. 7). We also find that the higher the SFE (SFR/M_{H_2}), the higher the $L'(^{12}CO)/L'(^{13}CO)$ line luminosity ratio, following an expected similar trend as with SFR. By looking at the stacked signals, we find significant variations of the $L'(^{12}CO)/L'(^{13}CO)$ line luminosity ratio when we split our sample by low and high SFR values (see Table 7). We notice that galaxies with high SFR not only show high $L'(^{12}CO)/L'(^{13}CO)$ luminosity ratio, but also show relatively high reservoirs of molecular gas. Table 7 shows the average values of redshift, molecular gas mass (M_{H_2}), molecular gas mass to stellar mass ratio ($M_{H_2}/M_\star$), and molecular gas fraction ($f_{H_2} = M_{H_2} / (M_{H_2}+M_\star)$) for our galaxy sample after splitting it in low and high SFR values. To estimate the significance of the observed differences between

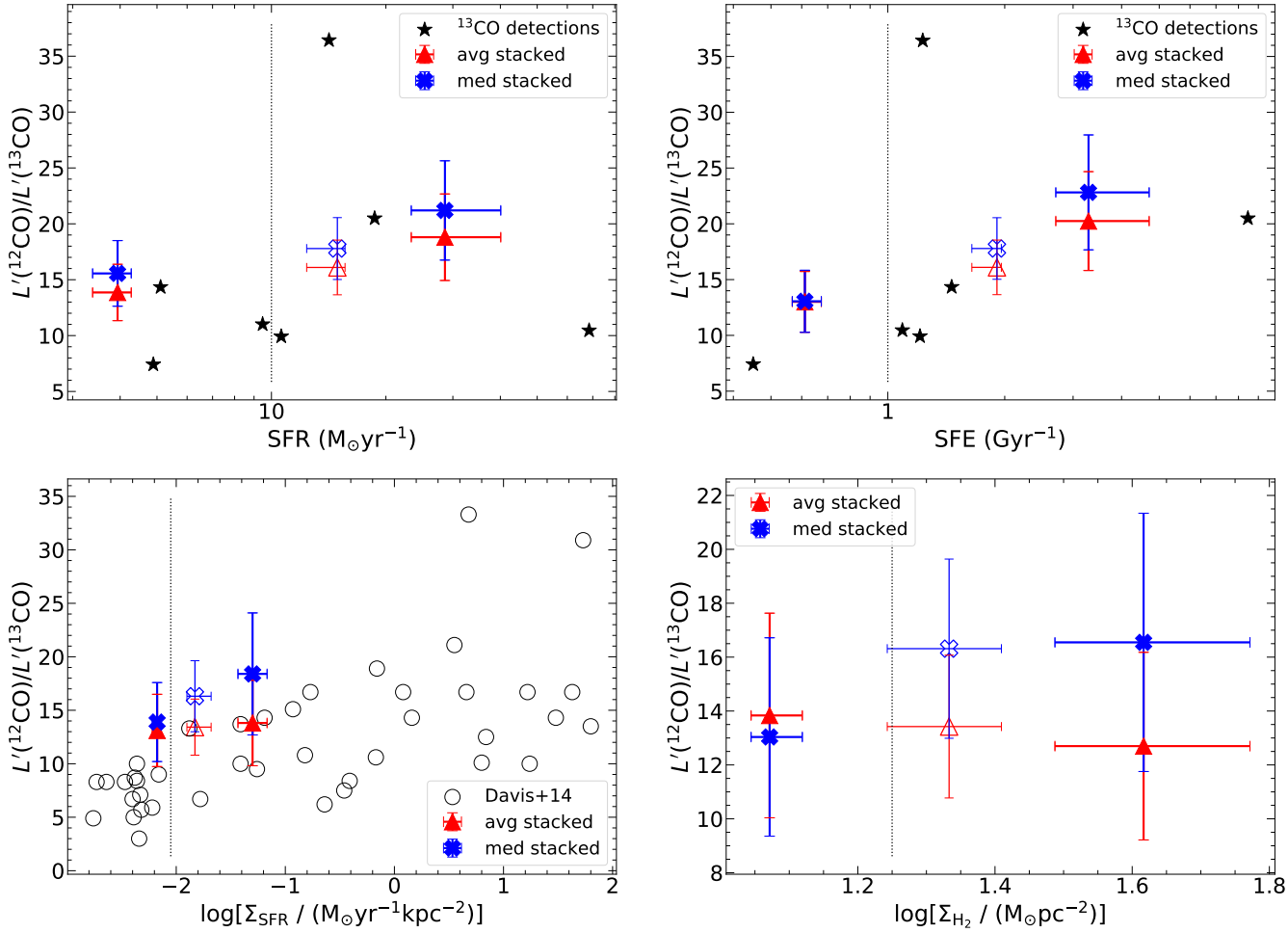

Figure 8. Average (red triangles) and median (blue crosses) stacked $L'(^{12}CO)/L'(^{13}CO)$ line luminosity ratio for low and high SFR (upper left), SFE (upper right), Σ_{SFR} (lower left) and Σ_{H_2} (lower right) subsets (triangles). As reference average and median line luminosity ratio considering all galaxies in open symbols and dashed lines indicating the boundary between low and high SFR, SFE, Σ_{SFR} and Σ_{H_2} populations are included. Error bars correspond to 1σ confidence intervals for average or median values based on Monte-Carlo simulations. Individual ^{13}CO detections (stars) and $I(^{12}CO)/I(^{13}CO)$ line intensity ratio of normal galaxies (open circles) from Davis (2014) are also included.

the average properties (M_{H_2}, $M_{H_2}/M_\star$, f_{H_2}) in the low and high SFR populations, we applied a Kolmogorov-Smirnov (KS) test to compute the probability that low and high (z, $M_{H_2}/M_\star$, $M_{H_2}/M_\star$ and f_{H_2}) distributions were drawn from from the same parent population. A large p-value indicates that the distributions are identical, while a small one suggests that the distributions are different. In all cases we find evidence to reject the null hypothesis that the observed properties in the low and high SFR populations were drawn from the same parent population (see Table 7).

We perform a similar analysis to that described by Davis (2014) that reported a positive correlation of the $I(^{12}CO)/I(^{13}CO)$ line intensity ratio with Σ_{SFR} and Σ_{H_2}. In our case only 13 galaxies are known to be resolved in ^{12}CO, enabling us to derive Σ_{SFR} and Σ_{H_2}. In Figure 8 (lower panels) we show the $L'(^{12}CO)/L'(^{13}CO)$ line luminosity ratio as a function of Σ_{SFR} split in high ($10^{-2.1}$–$10^{-1}\,M_\odot yr^{-1}\,kpc^{-2}$) and low ($10^{-2.6}$–$10^{-2}\,M_\odot yr^{-1}\,kpc^{-2}$) values. Individual ^{13}CO galaxy detections from Davis

Table 7. Average values of various galaxy parameters (Column 1): redshift, molecular gas mass (M_{H_2}), molecular gas mass to stellar mass ratio ($M_{H_2}/M_\star$), and molecular gas fraction (f_{H_2} = M_{H_2} / (M_{H_2}+$M_\star$)) for the sample after splitting it in low (Column 2) and high (Columns 3) SFR values. Columns 4 and 5 contain the Kolmogorov-Smirnov statistical reports (D, p) to asses the probability that low and high (z, $M_{H_2}/M_\star$ and f_{H_2}) were drawn from populations with identical distributions.

	SFR [$M_\odot yr^{-1}$]			
Parameter	low	high	KS	
	N = 15	N = 12	D	p
	[1.8-9.5]	[10.3-83.4]		
1	2	3	4	5
<z>	0.04 ± 0.01	0.10 ± 0.04	0.8	0.0001
<log[$M_{H_2}/M_\odot$]>	8.9 ± 0.6	10.1 ± 0.1	0.5	0.03
<$M_{H_2}/M_\star$>	0.17 ± 0.04	0.53 ± 0.18	0.6	0.02
<f_{H_2}>	0.14 ± 0.06	0.28 ± 0.15	0.55	0.02

(2014) are also over-plotted. Concerning the dependencies of $L'(^{12}\mathrm{CO})/L'(^{13}\mathrm{CO})$ as a function of Σ_{H_2}, when we split by low ($10^{0.8}$–$10^{1.3}$ $M_\odot$ pc^{-2}) and high ($10^{1.3}$–10^{-2} $M_\odot$ pc^{-2}) values, a moderate trend is found.

We applied a Student's t-test to evaluate the probability that the null hypothesis (i.e. that the $L'(^{12}\mathrm{CO})/L'(^{13}\mathrm{CO})$ line luminosity ratio variations between the low and high SFR, SFE, Σ_{SFR} and Σ_{H_2} populations are not statistically significant), is true. We find supporting evidence that $L'(^{12}\mathrm{CO})/L'(^{13}\mathrm{CO})$ variations between low and high SFR and SFE populations are statistically significant. On the other hand we do not find evidence that supports that $L'(^{12}\mathrm{CO})/L'(^{13}\mathrm{CO})$ variations between low and high Σ_{SFR}, Σ_{H_2} populations are not statistically significant (see Table 5). The lack of a significant difference of $L'(^{12}\mathrm{CO})/L'(^{13}\mathrm{CO})$ with both Σ_{SFR} and Σ_{H_2} shown in the lower panels of Figure 8 is most probably due to the reduced number of galaxies used for Σ_{SFR} and Σ_{H_2} stacks and the relatively small range of surface densities explored in this work. Finally, we note that we did not find any significant variations of $L'(^{12}\mathrm{CO})/L'(^{13}\mathrm{CO})$ with redshift and stellar mass, as with Σ_{H_2}. This might be caused by the relatively small range of redshift ([0.025-0.195]) and stellar masses ($\log(M/M_\odot)$=9.8-10.9) explored in this work.

4.1.3 ^{13}CO Individual detections

We have included the $L'(^{12}\mathrm{CO})/L'(^{13}\mathrm{CO})$ line luminosity ratios of the individual ^{13}CO detections (see Table 2) in Figures 5, 7, and 8. Galaxy J085748.0+004641 is classified as merger (M) while galaxy J083831.8+000044 is classified as a galaxy with a projected companion (DBC), they both show high $L'(^{12}\mathrm{CO})/L'(^{13}\mathrm{CO})$ line luminosity ratios, in good agreement with previous findings. On the other hand, galaxies J085346.4+001252, J084139.6+015346, J084350.8+005534 and J090633.6+001526 are classified as galaxies that do not show any apparent projected companion and present low $L'(^{12}\mathrm{CO})/L'(^{13}\mathrm{CO})$ line luminosity ratios, in agreement with those expected from galaxies with low L_{IR} values. Finally, galaxy J090949.6+014847 seems to be a peculiar galaxy showing a low $L'(^{12}\mathrm{CO})/L'(^{13}\mathrm{CO})$ line luminosity ratio but with low SFE = 1 Gyr^{-1} and high $L_{IR} = 10^{12}$ $L_\odot$ values. Thus, we identify J090949.6+014847 as an outlier and exclude it from the Spearman rank tests in the previous analyses. Stacking results are robust against the removal of this peculiar source from the sample.

4.1.4 110.201 GHz stacked continuum emission.

As discussed in section 2.2 we do not detect continuum emission at ~110GHz above 5σ significance down to a rms noise of 4μJy beam^{-1} in any of the 27 galaxies of our sample. However, we could detect a high signal-to-noise ratio (SNR=13) emission after stacking the individual continuum emission of our 27 galaxy sample coming from the ^{13}CO datasets. As with the ^{12}CO, ^{13}CO and C^{18}O stacks, we split our sample by low and high SFR populations (see Table 8). Similar to what we found for the $L'(^{12}\mathrm{CO})/L'(^{13}\mathrm{CO})$ ratio, galaxies with higher SFR show the higher continuum emission compared with galaxies with low SFR. The detected continuum emission does not show any discrepancy with the expected average continuum emission at ~110 GHz extrapolated from the spectral energy distributions presented in Villanueva et al. (2017). However further analyses (beyond the scope of this paper) at these frequencies are needed to uncover the origin of the continuum emission (*e.g. free-free, dust, ionized gas emission*) contributing to the SEDs of these galaxies and its relation with their star formation activity.

Table 8. ^{13}CO stacked continuum emission split by low and high SFR populations.

	SFR [$M_\odot$yr^{-1}]		
Parameter	All	low	high
	N = 27	N = 15	N = 12
		[1.8-9.5]	[10.3-83.4]
SNR	13	6	15
$S_{^{13}CO}\Delta v$ [μJy km s^{-1}]	82 ± 6	64 ± 10	110 ± 7

4.2 $L'(^{13}\mathrm{CO})/L'(\mathrm{C}^{18}\mathrm{O})$ correlations.

Our ALMA Band-3 observations helped with the exploration of the C^{18}O(1 – 0) emission line for 24 VALES galaxies. Following a similar approach as before, in this section we only use these 24 galaxies with simultaneous C^{18}O, ^{13}CO and ^{12}CO observations. Figures 9 and 10 show the trends for $L'(^{12}\mathrm{CO})/L'(^{13}\mathrm{CO})$ and $L'(^{13}\mathrm{CO})/L'(\mathrm{C}^{18}\mathrm{O})$ as a function of L_{IR}, SFR and SFE respectively and Table 9 for average $L'(^{12}\mathrm{CO})/L'(^{13}\mathrm{CO})$ and $L'(^{13}\mathrm{CO})/L'(\mathrm{C}^{18}\mathrm{O})$ values. The average $L'(^{13}\mathrm{CO})/L'(\mathrm{C}^{18}\mathrm{O})$ line luminosity ratio found is 2.5±0.6, which is in good agreement with the $I(^{13}\mathrm{CO})/I(\mathrm{C}^{18}\mathrm{O})$ line intensity ratio found for starburst galaxies (3.4±0.9) but slightly lower than the average ratio found in nearby normal spiral galaxies (6.0±0.9) reported by Jiménez-Donaire et al. (2017). The central panel of Figure 10 shows the $L'(^{13}\mathrm{CO})/L'(\mathrm{C}^{18}\mathrm{O})$ line luminosity ratio as a function of SFR (see Table 10) and also includes values reported in the literature gathered by Romano et al. 2017 and split by normal, starburts and ultra luminous infrarred galaxies (ULIRGs).

As with $L'(^{12}\mathrm{CO})/L'(^{13}\mathrm{CO})$ trends discussed in Section 4.1 we implemented a Student's t-test to evaluate the significance of the $L'(^{12}\mathrm{CO})/L'(^{13}\mathrm{CO})$ and $L'(^{13}\mathrm{CO})/L'(\mathrm{C}^{18}\mathrm{O})$ variations with L_{IR}, SFR and SFE considering the 24 galaxies with C^{18}O coverage. We find that the differences found in the $L'(^{12}\mathrm{CO})/L'(^{13}\mathrm{CO})$ and $L'(^{13}\mathrm{CO})/L'(\mathrm{C}^{18}\mathrm{O})$ variations between low and high L_{IR}, SFR, SFE populations are statistically significant (see Table 9). We also applied a KS test to assess the probability that the null hypothesis (low and high: SFR, SFE, L_{IR}, $M_{H_2}/M_\odot$, $M_{H_2}/M_\star$, and f_{H_2} populations were drawn from the same parent population) is true, considering the reduced 24 galaxy sample with C^{18}O coverage. Table 10 shows the average values of redshift, $M_{H_2}/M_\odot$, $M_{H_2}/M_\star$), and f_{H_2} split by low and high SFR values and the Kolmogorov-Smirnov statistics (D, p). We find supporting evidence to reject the null hypothesis that the low and high SFR populations were drawn from the same parent population. Therefore, galaxies with high $L'(^{12}\mathrm{CO})/L'(^{13}\mathrm{CO})$ ratio (Figure 9) and low $L'(^{13}\mathrm{CO})/L'(\mathrm{C}^{18}\mathrm{O})$ ratio (Figure 10) also show relatively

Table 9. Average $L'(^{12}CO)/L'(^{13}CO)$ and $L'(^{13}CO)/L'(C^{18}O)$ line luminosity ratios for the sample of 24 VALES galaxies with $C^{18}O$ observations split by low and high L_{IR}, SFR, SFE, values (see Figs. 9 and 10). Column 1: Parameter of interest; Column 2: Range explored; Column 3: Number of galaxies in the explored range; Column 4: Average value for parameter of interest; Columns 5 and 8: The average stacked $L'(^{12}CO)/L'(^{13}CO)$ and $L'(^{13}CO)/L'(C^{18}O)$ line luminosity ratios respectively. Finally the Student's t-test statistical reports (t, p) to asses the probability that the null hypothesis ($L'(^{12}CO)/L'(^{13}CO)$ and $L'(^{13}CO)/L'(C^{18}O)$ line luminosity ratios variations between low and high L_{IR}, SFR, SFE populations are not statistically significant) is true, located in Columns 6 and 9 (t coefficient) and Columns 7 and 10 (probability p-value) respectively.

Parameter	Range	N	Average	$L'(^{12}CO)/L'(^{13}CO)$	t-test		$L'(^{13}CO)/L'(C^{18}O)$	t-test	
					t	p		t	p
1	2	3	4	5	6	7	8	9	10
$\log[L_{IR}/L_\odot]$	[10.1 - 11.0]	13	10.5 ± 0.1	13.0 ± 2.5	-4.4	0.002	3.3 ± 0.8	-2.8	0.01
	[11.1 - 11.8]	11	11.3 ± 0.1	18.8 ± 3.7			2.5 ± 0.6		
SFR ($M_\odot yr^{-1}$)	[1.3 - 9.5]	13	3.7 ± 0.5	13.0 ± 2.6	-4.2	0.0003	3.3 ± 0.8	-2.8	0.01
	[10.3 - 68.5]	11	23.6 ± 4.0	18.8 ± 3.8			2.5 ± 0.6		
SFE (Gyr^{-1})	[0.4 - 0.9]	11	0.6 ± 0.1	12.4 ± 2.8	-4.8	7E-5	4.4 ± 1.2	-5.9	5E-6
	[1.1 - 11.8]	13	3.3 ± 0.6	19.4 ± 4.2			2.1 ± 0.5		

Table 10. Average values of different parameters (Column 1): redshift, molecular gas mass (M_{H_2}), molecular gas mass to stellar mass ratio ($M_{H_2}/M_\star$), and molecular gas fraction ($f_{H_2} = M_{H_2} / (M_{H_2}+M_\star)$) considering 24 galaxies with $C^{18}O$ coverage split by low (Column 2) and high SFR values (Column 3) . Columns 4 and 5 contain the Kolmogorov-Smirnov statistical reports (D, p) to asses the probability that low and high (z, M_{H_2}, $M_{H_2}/M_\star$, and f_{H_2}) populations were drawn from populations with identical distributions.

	SFR [$M_\odot yr^{-1}$]			
Parameter	low	high	KS	
	N = 15	N = 12	D	p
	[1.3-9.5]	[10.3-68.5]		
1	2	3	4	5
<z>	0.04 ± 0.01	0.10 ± 0.04	0.8	7E-5
$<\log[M_{H_2}/M_\odot]>$	8.8 ± 0.1	9.9 ± 0.1	0.8	0.01
$<M_{H_2}/M_\star>$	0.15 ± 0.04	0.36 ± 0.05	0.6	0.02
$<f_{H_2}>$	0.12 ± 0.07	0.24 ± 0.09	0.6	0.02

high L_{IR}, SFR, SFE and high reservoirs of molecular gas (see Table 10). These line ratios can be explained by over-abundances of ^{12}CO and $C^{18}O$ (both produced in high mass stars), with respect ^{13}CO, that could be understood as a result of selective nucleosynthesis where high-mass stars enrich the ISM of these galaxies.

5 DISCUSSION

The $L'(^{12}CO)/L'(^{13}CO)$ line luminosity ratios presented in this work can be affected by optical depth effects or by the different physical processes that have been invoked to explain large and low $I(^{12}CO)/I(^{13}CO)$ line intensity ratios. The most relevant ones are: i) selective photodissociation: ^{12}CO molecules are more abundant than ^{13}CO molecules and hence due to their higher density they are self-shielded against strong interstellar UV radiation fields, unlike less abundant ^{13}CO molecules which are more easily photo-dissociated leading to a ^{13}CO under abundance and hence a higher $I(^{12}CO)/I(^{13}CO)$ line intensity ratio in regions with strong UV radiation fields, ii) chemical isotope-dependent fractionation: where gas kinetic temperatures elevates ^{13}CO abundance through the isotopic charge exchange reaction (Watson 1977), where $^{12}CO + {}^{13}C^+ \rightarrow {}^{12}C^+ + {}^{13}CO + \Delta E$ and iii) selective nucleosynthesis where massive stars in star forming regions produce significantly higher amounts of ^{12}C compared to ^{13}C leading to a high $I(^{12}CO)/I(^{13}CO)$ line intensity ratio (Henkel & Mauersberger 1993; Aalto et al. 1995).

The higher $L'(^{12}CO)/L'(^{13}CO)$ line luminosity ratio found for galaxies with close companions may be explained by interaction activity. For example, during the early stages of a merger event, part of the gas escapes and disperses into the intergalactic medium (Mirabel, & Sanders 1989). The remaining gas shrinks to the center, becomes denser and converted partially into molecular H_2 gas. This fresh molecular gas with relatively low metallicity and hence a high $^{12}C/^{13}C$ luminosity ratio will trigger new starburst events boosting the $^{12}CO/^{13}CO$ abundance ratio (Casoli et al. 1992b; Langer & Penzias 1990). On the other hand, the opposite scenario occurs in galaxies in denser environments, like galaxy clusters, where a deficit in ^{12}CO is linked to the low $I(^{12}CO)/I(^{13}CO)$ line ratios observed. Galaxies in clusters have lived long enough to enrich the ISM with ^{13}C atoms from low mass stellar nucleosynthesis, while at the same time, the evaporation or stripping of low density GMCs as galaxies enter into the cluster moving through the intracluster medium (ICM), possibly reduce the presence of new starburst events and therefore would lead to a reduced $I(^{12}CO)/I(^{13}CO)$ intensity ratio (Alatalo et al. 2015). In summary, the enhanced $L'(^{12}CO)/L'(^{13}CO)$ line luminosity ratios observed in galaxy mergers (M) and galaxies with a projected companion (BC, DC) which got relatively high SFR (34±6.9 and 17.6±5.9, respectively) could be explained by a new starburst activity in these systems. Galaxies without any projected companion (B, D) with low SFRs present a relatively low $L'(^{12}CO)/L'(^{13}CO) = 3.4\pm0.5$ line luminosity ratio, which could be explained by ^{13}C enrichment of their ISM induced by low and intermediate mass stars in the absence of young starburst events.

The trends of $L'(^{12}CO)/L'(^{13}CO)$ with L_{IR}, SFR, and

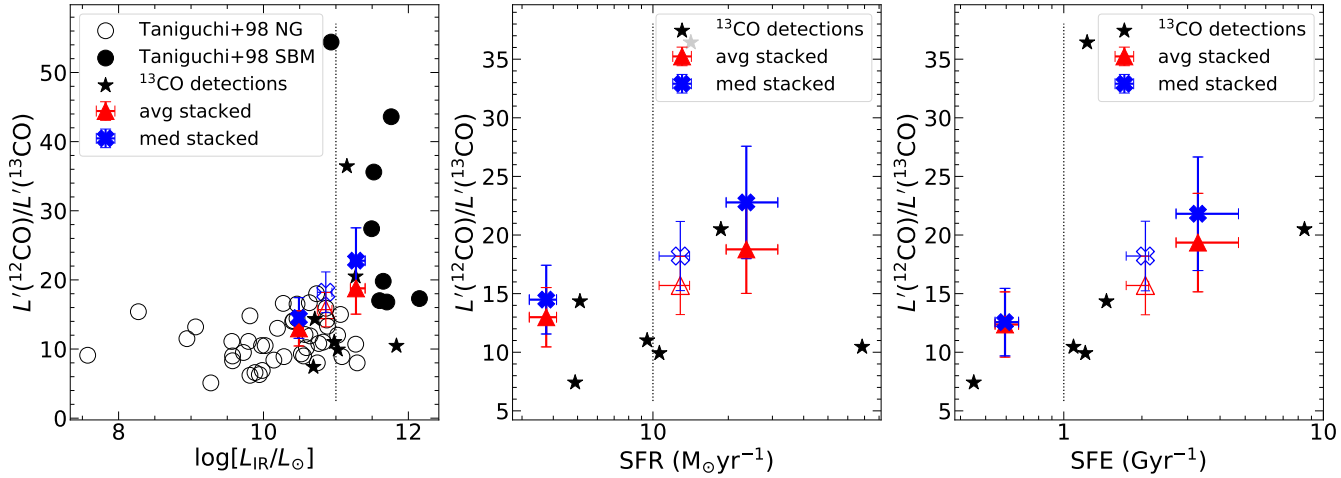

Figure 9. Average (red triangles) stacked $L'(^{12}CO)/L'(^{13}CO)$ line luminosity ratio for low and high L_{IR} (left panel), SFR (middle panel) and SFE (right panel), subsets (triangles). As reference average and median line luminosity ratio considering all galaxies in open symbols and dashed lines indicating the boundary between low and high L_{IR}, SFR and SFE populations are included. Error bars correspond to 1σ confidence intervals for average (or median) values based on Monte-Carlo simulations. $L'(^{12}CO)/L'(^{13}CO)$ line ratios of normal galaxies (open circles), starburst mergers (filled circles) scaled by a 1.75 factor to convert from far-IR to IR luminosities (see Appendix E from Herrera-Camus et al. 2015). Data from Taniguchi & Ohyama (1998) and individual ^{13}CO detections (stars) are also included.

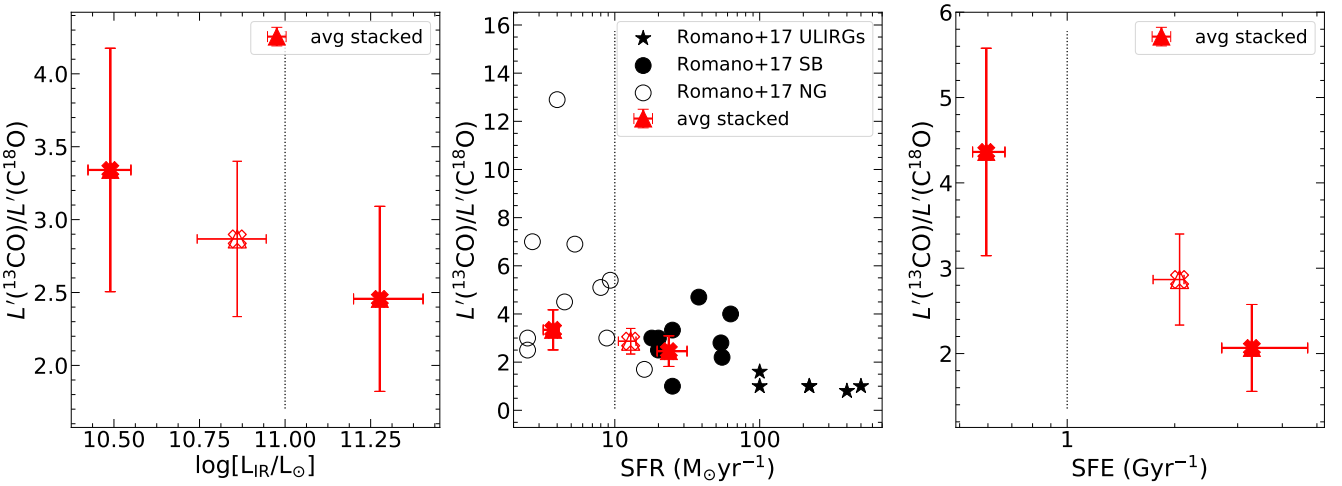

Figure 10. Average (red triangles) stacked $L'(^{13}CO)/L'(C^{18}O)$ line luminosity ratio for low and high L_{IR} (levt panel), SFR (middle panel) and SFE (right panel), subsets (triangles). As reference average line luminosity ratio considering all 24 galaxies with $C^{18}O$ coverage are shown in open symbols and dashed lines indicating the boundary between low and high L_{IR}, SFR and SFE populations are included. Error bars correspond to 1σ confidence intervals for average values based on Monte-Carlo simulations. $I(^{13}CO)/I(C^{18}O)$ ratios reported in the literature and gathered by (Romano et al. 2017) split by normal galaxies (NG open circles), starburst galaxies (SB filled circles) and ULIRGs (stars) as a function of SFR are also included. We note that median $L'(^{13}CO)/L'(C^{18}O)$ line luminosities stacks are not included in our analyses due to low significance in these values.

SFE (see Figures 7, 8 and 9) found in this work provide the evidence that galaxies with low SFR, SFE and L_{IR}, also show low $L'(^{12}CO)/L'(^{13}CO)$ line luminosity ratios in agreement to the idea that normal star forming galaxies have larger gas consumption times to enrich with ^{13}C the ISM from low and intermediate mass stars. On the other hand galaxies with high SFR, SFE and L_{IR} present high $L'(^{12}CO)/L'(^{13}CO)$ line luminosity ratios most probably due to younger starburst activity. These higher ratios found here are in good agreement with scenarios in which galaxies with higher fractions of dense molecular gas (see Tables 7 and 10) show higher L_{IR} and higher SFE (Solomon & Vanden Bout 2005; Solomon et al. 1992), probably induced by the triggering of a recent starburst episode after the in-fall of unprocessed gas to the central galaxy regions (Henkel & Mauersberger 1993; Casoli et al. 1992a; König et al. 2016).

Similarly, the $I(^{13}CO)/I(C^{18}O)$ line intensity ratios are explained in terms of either a ^{13}CO deficit or an over-

abundance of $C^{18}O$. Recently, low $I(^{13}CO)/I(C^{18}O)$ line intensity ratios have been reported for different type of galaxies Danielson et al. (2013); Sliwa et al. (2017); Jiménez-Donaire et al. (2017); Brown & Wilson (2019). In all these cases, the low ratios have been attributed to the presence of massive stars in a recent starburst. Our trends found for $L'(^{13}CO)/L'(C^{18}O)$ (Figure 10) are in good agreement to previous ratios reported for starburst galaxies (Zhang et al. 2018; Jiménez-Donaire et al. 2017). Considering the 24 VALES galaxies with $C^{18}O$ spectral coverage, we show moderate trends of $L'(^{13}CO)/L'(C^{18}O)$ with L_{IR}, SFR, and SFE. Galaxies with higher L_{IR}, SFR and SFE are found to show high $L'(^{12}CO)/L'(^{13}CO)$ (Figure 9), low $L'(^{13}CO)/L'(C^{18}O)$ (Figure 10) luminosity ratios, and relatively high reservoirs of molecular gas (see Table 10). Similar results have been associated to a top heavy IMF (Danielson et al. 2013; Sliwa et al. 2017; Zhang et al. 2018; Brown & Wilson 2019), however in order to break the degeneracy between young starburst and top-heavy IMF, an independent determination of the age of the starburst is needed.

5.1 Optical depth, selective photodissociation and chemical fractionation effects.

Aalto et al. (1995) pointed out the difficulties from interpreting the ^{12}CO and ^{13}CO abundances from $I(^{12}CO)/I(^{13}CO)$ line intensity ratios as these might be affected by surface density, optical depth, and gas temperature. They suggested that the high $I(^{12}CO)/I(^{13}CO)$ line intensity ratios observed in mergers and interacting galaxies (Casoli et al. 1992b; Henkel & Mauersberger 1993) is produced by the in-falling of unprocessed gas which could affect the gas elemental abundances, only if the ISM has moderate optical depths ($\tau \approx 1$). More recently, Zhang et al. (2018) presented how ^{13}CO and $C^{18}O$ opacity affects $I(^{12}CO)/I(^{13}CO)$ and $I(^{13}CO)/I(C^{18}O)$ line intensity ratios in local thermodynamic equilibrium (LTE) and non LTE conditions assuming: representative Galactic abundance ratios ($^{13}CO/C^{18}O$ = 7–10, $^{12}CO/^{13}CO$=70), and typical ULIRGs and SMGs conditions (*e.g.* $\tau_{^{12}CO} \approx 2$, T_{kin} = 30K). They found that the high $I(^{12}CO)/I(^{13}CO)$ ratios $\geq$ 30 observed in high redshift galaxies, would need extremely low optical depths for ^{13}CO ($\tau < 0.03$), meaning that $I(^{12}CO)/I(^{13}CO)$ line intensity ratios are affected by optical depth effects. In order to properly account the optical depths in $I(^{12}CO)/I(^{13}CO)$ intensity ratios, multiple line transitions observations are needed to measure excitation conditions and derive the optical depths of the ISM in these galaxies, which is beyond the scope this work and hence, the $L'(^{12}CO)/L'(^{13}CO)$ luminosity ratios reported here should be taken as a lower limit of the $^{12}CO/^{13}CO$ abundance ratio (Henkel et al. 2010; Martín et al. 2019). On the other hand, Zhang et al. (2018) found that even moderate ^{13}CO optical depths ($\tau_{^{13}CO} \sim$ 0.2-0.5) do not cause the $I(^{13}CO)/I(C^{18}O)$ line intensity ratio to deviate significantly from more typical values ($^{13}CO/C^{18}O$~7), meaning that the low $I(^{13}CO)/I(C^{18}O)$ found in high-redshift starbursts and local ULIRGs reflect the intrinsic isotopologue abundance ratios (*i.e.* $I(^{13}CO)/I(C^{18}O) \approx {}^{13}CO/C^{18}O \approx {}^{13}C/{}^{18}O$).

If chemical fractionation is the main physical mechanism controlling the observed line ratios, the ^{13}CO abundance would be boosted with respect to ^{12}CO (and $C^{18}O$) at low temperatures (T $\approx$ 10 K Watson, Anicich & Huntress 1976). Nevertheless, considering a mean temperature T $>$ 20 K (Ibar et al. 2015; Hughes et al. 2017) for our VALES sample, we can reject chemical fractionation as the main mechanism controlling the $L'(^{12}CO)/L'(^{13}CO)$ ratios. On the other hand, selective photodissociation can affect the less abundant ^{13}CO and $C^{18}O$ molecules compared to ^{12}CO, however extreme conditions with high gas densities ($> 10^{26}cm^{-3}$) are required (Zhang et al. 2018; Romano et al. 2017). However with an average gas density of 10^4cm^{-3} (Hughes et al. 2017), our sample of galaxies do not fulfill such conditions. Moreover, knowing that $C^{18}O$ is even more sensitive to selective dissociation than ^{13}CO, $C^{18}O$ molecules would be more dissociated than ^{13}CO molecules, resulting in high $L'(^{13}CO)/L'(C^{18}O)$ ratios, which is inconsistent with results shown in Figure 10 where galaxies with more intense UV radiation fields associated with high L_{IR} and SFR show low $L'(^{13}CO)/L'(C^{18}O)$ ratios. Thus, the $(L'^{12}CO)/(L'^{13}CO)$ and $(L'^{13}CO)/L'(C^{18}O)$ variations found here are not compatible with a scenario in which selective photodissociation or chemical fractionation play a dominant role.

5.2 Insights from Galactic Chemical Evolution

Recently Romano et al. (2017) used Galactic Chemical Evolution (GCE) models to compute the the abundances of numerous elements including ^{12}C, ^{16}O, ^{13}C and ^{18}O in the ISM of galaxies, assuming that i) stars form from raw material with primordial chemical composition, ii) outflows remove stellar ejecta and a fraction of the surrounding ISM, iii) star formation follows a canonical Kennicutt-Schmidt law (Schmidt 1959; Kennicutt 1998), iv) stars release the synthesized elements during their lifetime, and v) stellar eject are homogeneously mixed in the ISM, allowing to follow multiple isotopic ratios and trace their abundance ratios on different isotopes and different elements. They have shown that neither selective photodissociation nor chemical isotope-dependent fractionation can significantly perturb globally averaged isotopologue abundance ratios, since these processes will typically affect only small mass fractions of individual molecular clouds in galaxies. Using these models Zhang et al. (2018) was able to compare the effects of assuming different IMF of young starbursts by incorporating the appropriate timescales at which different stellar populations enrich the ISM, and conclude that a canonical IMF can not reproduce the observed low $I(^{13}CO)/I(C^{18}O)$ ratios in ULIRGs and SMGs. Thus assuming that the velocity integrated line flux densities coming from average stacks are not affected by these two other effects, we propose that these emission line ratios could be induced by selective nucleosynthesis.

6 CONCLUSIONS

In this paper we present a stacking analysis of $^{12}CO(1-0)$, $^{13}CO(1-0)$ emission lines of 27 galaxies, and $C^{18}O$ (1 – 0) in 24 galaxies, belonging to the VALES survey. We have detected 6 individual ^{13}CO (1-0) line signals from 6 galaxies in moment-0 maps, with SNR $>$ 5. We have successfully demonstrated that it is possible to detect the signal

coming from faint emission lines (^{13}CO and C^{18}O) in low-redshift galaxies through stacking analysis, pushing the current ALMA detectability limits. Therefore, the analysis presented here can be applied to detect faint signals from different molecules coming from low, intermediate and high redshift galaxies, exploiting radio interferometric datasets from ALMA.

We have explored three different independent stacking analysis, two of them in the "image plane" i) 2D-moment-0 stacking and ii) 3D-image stacking, while a third one in visibility's space iii) *uv*-plane stacking. We found that for bright emission line (as the case for ^{12}CO) *uv*-plane stacks produce the highest signal-to-noise compared to 2D-moment-0, and 3D-image stacks. Moment-zero stacked maps for faint lines, like ^{13}CO, shows the highest signal to noise compared with 3D-image and *uv*-plane stackings.

We found an overall $L'(^{12}\mathrm{CO})/L'(^{13}\mathrm{CO})$ line luminosity ratio of 16.1±2.5. We also found a dependence of $L'(^{12}\mathrm{CO})/L'(^{13}\mathrm{CO})$ line luminosity ratio on optical morphology/environment where galaxies showing a close projected companion and mergers show boosted $L'(^{12}\mathrm{CO})/L'(^{13}\mathrm{CO})$ line luminosity ratios. Mergers show at low significance a $L'(^{12}\mathrm{CO})/L'(^{13}\mathrm{CO})$ line luminosity ratio which is 2 times higher than that found in galaxies without a projected companion. We also found positive trends between $L'(^{12}\mathrm{CO})/L'(^{13}\mathrm{CO})$ line luminosity ratio and SFR, SFE, L_{IR}, $\Sigma_{\mathrm{H_2}}$ and Σ_{SFR}.

We also provide C^{18}O stacking analysis for 24 VALES galaxies. We detect signal coming from the 2D moment-0 stacked images at a significance of $\sim 5\sigma$ with an average $L'(^{13}\mathrm{CO})/L'(\mathrm{C}^{18}\mathrm{O})$ line luminosity ratio of 2.5±0.6. This average value is in good agreement to the $I(^{13}\mathrm{CO})/I(\mathrm{C}^{18}\mathrm{O}) = 3.4\pm0.9$ line ratio for starburst galaxies found by Jiménez-Donaire et al. (2017). We find negative trends of $L'(^{13}\mathrm{CO})/L'(\mathrm{C}^{18}\mathrm{O})$ as a function of L_{IR}, SFR and SFE.

We recall that our $\mathrm{L'}(^{12}\mathrm{CO})/\mathrm{L'}(^{13}\mathrm{CO})$ ratios can be affected by optical depth effects, and hence the $L'(^{12}\mathrm{CO})/L'(^{13}\mathrm{CO})$ luminosity ratios reported here should be taken as a lower limit for the ^{12}CO/^{13}CO abundance ratio. To assess the optical depth effects on $I(^{12}\mathrm{CO})/I(^{13}\mathrm{CO})$ intensity ratios, multiple line transitions observations are needed to measure excitation conditions and derive the optical depths of the ISM.

Neither chemical fractionation nor selective photodissociation are expected to be responsible for the trends found in this work as the required low temperatures ($\leq 10K$) and high densities ($> 10^{26}\mathrm{cm}^{-3}$) are not fulfilled by our sample of galaxies. The combined $L'(^{12}\mathrm{CO})/L'(^{13}\mathrm{CO})$ and $L'(^{13}\mathrm{CO})/L'(\mathrm{C}^{18}\mathrm{O})$ variations provide additional evidence inconsistent with selective photodissociation as the responsible agents behind the results shown here. This, leaves selective nucleosythesis to be the most probable mechanism for the high $L'(^{12}\mathrm{CO})/L'(^{13}\mathrm{CO})$ and low $L'(^{13}\mathrm{CO})/L'(\mathrm{C}^{18}\mathrm{O})$ ratios found in bright far-IR luminosity galaxies. The scenario might be that higher molecular gas reservoirs can trigger new starburst events where high mass stars enrich their ISM.

Future analyses using ALMA observations of these and other CNO isotoplogue molecules (C^{17}O, ^{12}CN, ^{13}CN) on larger samples, sampling different galaxy populations covering wider ranges in SFR, SFE, and molecular gas contents at different epochs could fill in the gap of these molecular line observations between nearby galaxies and lensed galaxies at high redshift, shedding light on the physical processes behind their star formation activity.

ACKNOWLEDGEMENTS

We thank an anonymous referee for constructive comments and suggestions, which helped to improve the manuscript. HMH and EI acknowledge partial support from FONDECYT through grant N°:1171710. M.J.M. acknowledges the support of the National Science Centre, Poland through the SONATA BIS grant 2018/30/E/ST9/00208. KKK acknowledges support from the Swedish Research Council (2015-05580). This work also benefited from the International Space Science Institute (ISSI/ISSI-BJ) in Bern and Beijing, thanks to the funding of the team "Chemical abundances in the ISM: the litmus test of stellar IMF variations in galaxies across cosmic time" (Principal Investigator D.R. and Z-Y.Z.). TMH acknowledges the support from the Chinese Academy of Sciences (CAS) and the National Commission for Scientific and Technological Research of Chile (CONICYT) through a CAS-CONICYT Joint Postdoctoral Fellowship administered by the CAS South America Center for Astronomy (CASSACA) in Santiago, Chile. This paper makes use of the following ALMA data: ADS/JAO.ALMA 2013.1.00530.S. ALMA is a partnership of ESO (representing its member states), NSF (USA) and NINS (Japan), together with NRC (Canada), NSC and ASIAA (Taiwan), and KASI (Republic of Korea), in cooperation with the Republic of Chile. The Joint ALMA Observatory is operated by ESO, AUI/NRAO and NAOJ. GAMA is a joint European-Australasian project based around a spectroscopic campaign using the Anglo-Australian Telescope. The GAMA input catalogue is based on data taken from the Sloan Digital Sky Survey and the UKIRT Infrared Deep Sky Survey. Complementary imaging of the GAMA regions is being obtained by a number of independent survey programmes including GALEX MIS, VST KiDS, VISTA VIKING, WISE, Herschel-ATLAS, GMRT and ASKAP providing UV to radio coverage. GAMA is funded by the STFC (UK), the ARC (Australia), the AAO, and the participating insti- tutions. The GAMA website is `http://www.gama-survey.org/`. This research made use of Astropy,[3] a community-developed core Python package for Astronomy (Astropy Collaboration et al. 2013, 2018).

DATA AVAILABILITY

The data underlying this article are available in the ALMA Science Archive at `https://almascience.nrao.edu/asax/`, and can be accessed with the Project ID: 2013.1.00530.S.

REFERENCES

Adelman-McCarthy J. K., et al., 2008, ApJS, 175, 297

[3] http://www.astropy.org

Alatalo, K., Crocker, A. F., Aalto, S., et al. 2015, MNRAS, 450, 3874
Aalto, S., Booth, R. S., Black, J. H., & Johansson, L. E. B. 1995, A&A, 300, 369
Astropy Collaboration, Robitaille, T. P., Tollerud, E. J., et al. 2013, A&A, 558, A33
Astropy Collaboration, Price-Whelan, A. M., Sipőcz, B. M., et al. 2018, AJ, 156, 123
Aalto S., Black J. H., Johansson L. E. B., Booth R. S., 1991, A&A, 249, 323
Bergin, E. A., & Tafalla, M. 2007, ARA&A, 45, 339
Béthermin, M., Kilbinger, M., Daddi, E., et al. 2014, A&A, 567, A103
Bolatto, A. D., Wolfire, M., & Leroy, A. K. 2013, ARA&A, 51, 207.
Brown T., Wilson C. D., 2019, ApJ, 879, 17
Bartelmann M., White S. D. M., 2003, A&A, 407, 845
Brandt W. N., et al., 2001, AJ, 122, 1
Berry M., et al., 2012, ApJ, 749, 4
Bera A., Kanekar N., Weiner B. J., Sethi S., Dwarakanath K. S., 2018, ApJ, 865, 39
Casoli, F., Dupraz, C., & Combes, F. 1992, A&A, 264, 49
Casoli, F., Dupraz, C., & Combes, F. 1992, A&A, 264, 55
Chabrier G., 2003, ApJL, 586, L133
Cheng, C., Ibar, E., Hughes, T. M., et al. 2018, MNRAS, 475, 248
Condon, J. J., & Ransom, S. M. 2016, Essential Radio Astronomy.
Cormier, D., Bigiel, F., Jiménez-Donaire, M. J., et al. 2018, MNRAS, 475, 3909
Carilli C. L., et al., 2008, ApJ, 689, 883
Carvajal R., et al., 2020, A&A, 633, A160
Danielson, A. L. R., Swinbank, A. M., Smail, I., et al. 2013, MNRAS, 436, 2793
Davis, T. A. 2014, MNRAS, 445, 2378
Driver, S. P., Wright, A. H., Andrews, S. K., et al. 2016, MNRAS, 455, 3911
Dunne, L., Gomez, H. L., da Cunha, E., et al. 2011, MNRAS, 417, 1510
Dole H., et al., 2006, A&A, 451, 417
Duivenvoorden S., et al., 2020, MNRAS, 491, 1355
Eales, S., Dunne, L., Clements, D., et al. 2010, PASP, 122, 499
Encrenaz, P. J., Stark, A. A., Combes, F., et al. 1979, A&A, 78, L1.
Evans, N. J. 1999, ARA&A, 37, 311
Fujimoto S., et al., 2019, ApJ, 887, 107
Fujimoto S., et al., 2018, ApJ, 861, 7
Fudamoto Y., et al., 2020, MNRAS, 491, 4724
Gao, Y., & Solomon, P. M. 2004, ApJ, 606, 271
Glenn, J., & Hunter, T. R. 2001, ApJS, 135, 177
Halfen, D. T., Woolf, N. J., & Ziurys, L. M. 2017, ApJ, 845, 158
Hardcastle, M. J., Gürkan, G., van Weeren, R. J., et al. 2016, MNRAS, 462, 1910
Henkel, C., & Mauersberger, R. 1993, A&A, 274, 730
Henkel, C., Downes, D., Weiß, A., et al. 2010, A&A, 516, A111.
Herwig, F., & Austin, S. M. 2004, ApJ, 613, L73
Hughes T. M., et al., 2017, A&A, 602, A49
Herrera-Camus R., et al., 2015, ApJ, 800, 1
Ibar E., et al., 2013, MNRAS, 434, 3218
Ibar, E., Lara-López, M. A., Herrera-Camus, R., et al. 2015, MNRAS, 449, 2498
Jiménez-Donaire, M. J., Cormier, D., Bigiel, F., et al. 2017, ApJ, 836, L29.
Kobayashi, C., Karakas, A. I., & Umeda, H. 2011, Monthly Notices of the Royal Astronomical Society, 414, 3231
König, S., Aalto, S., Muller, S., et al. 2016, A&A, 594, A70
Kennicutt, R. C. 1998, ApJ, 498, 541
Knudsen K. K., et al., 2005, ApJL, 632, L9
Lindroos, L., Knudsen, K. K., Vlemmings, W., Conway, J., & Martí-Vidal, I. 2015, MNRAS, 446, 3502
Langer, W. D., Graedel, T. E., Frerking, M. A., & Armentrout, P. B. 1984, ApJ, 277, 581
Langer, W. D., & Penzias, A. A. 1990, ApJ, 357, 477
Langer, W. D., & Penzias, A. A. 1993, ApJ, 408, 539
Liske, J., Baldry, I. K., Driver, S. P., et al. 2015, MNRAS, 452, 2087
Lehmer B. D., et al., 2007, ApJ, 657, 681
Lehmer B. D., et al., 2016, ApJ, 825, 7
Loomis, R. A., Öberg, K. I., Andrews, S. M., et al. 2018, AJ, 155, 182
Lindroos L., et al., 2016, MNRAS, 462, 1192
Martín, S., Muller, S., Henkel, C., et al. 2019, A&A, 624, A125
Milam, S. N., Savage, C., Brewster, M. A., et al. 2005, ApJ, 634, 1126.
Mirabel, I. F., & Sanders, D. B. 1989, ApJ, 340, L53
Narayanan D., Krumholz M. R., 2014, MNRAS, 442, 1411
Matrà L., Panić O., Wyatt M. C., Dent W. R. F., 2015, MNRAS, 447, 3936
Marino S., et al., 2016, MNRAS, 460, 2933
Miller N. A., et al., 2013, ApJS, 205, 13
Miller N. A., et al., 2008, ApJS, 179, 114
Millard J. S., et al., 2020, MNRAS.tmp, doi:10.1093/mnras/staa609
Pagel, B. E. J. 1997, Nucleosynthesis and Chemical Evolution of Galaxies, by Bernard E. J. Pagel, pp. 392. ISBN 0521550610. Cambridge, UK: Cambridge University Press, October 1997., 392
Penzias, A. A., Jefferts, K. B., & Wilson, R. W. 1971, ApJ, 165, 229.
Penzias, A. A. 1981, ApJ, 249, 518
Prantzos, N., Aubert, O., & Audouze, J. 1996, A&A, 309, 760.
Perger K., Frey S., Gabányi K. É., Tóth L. V., 2019, MNRAS, 490, 2542
Rickard, L. J., Palmer, P., Morris, M., et al. 1975, The Astrophysical Journal, 199, L75
Rickard, L. J., & Blitz, L. 1985, ApJ, 292, L57.
Romano, D., Matteucci, F., Zhang, Z.-Y., et al. 2017, MNRAS, 470, 401.
Rodighiero G., et al., 2015, ApJL, 800, L10
Rigby J. R., et al., 2018, ApJ, 853, 87
Sage, L. J., & Isbell, D. W. 1991, A&A, 247, 320.
Sliwa, K., Wilson, C. D., Matsushita, S., et al. 2017, ApJ, 840, 8.
Spilker, J. S., Marrone, D. P., Aguirre, J. E., et al. 2014, ApJ, 785, 149.
Solomon, P. M., Downes, D., & Radford, S. J. E. 1992, ApJ, 387, L55
Solomon, P. M., & Vanden Bout, P. A. 2005, ARA&A, 43, 677
Scoville N., et al., 2007, ApJS, 172, 1
Schinnerer E., et al., 2007, ApJS, 172, 46
Schmidt, M. 1959, ApJ, 129, 243
Tan, Q.-H., Gao, Y., Zhang, Z.-Y., & Xia, X.-Y. 2011, Research in Astronomy and Astrophysics, 11, 787
Taniguchi, Y., & Ohyama, Y. 1998, ApJ, 507, L121
Taniguchi, Y., Ohyama, Y., & Sanders, D. B. 1999, ApJ, 522, 214
Timmes F. X., Woosley S. E., Weaver T. A., 1995, ApJS, 98, 617
Tinsley, B. M. 1980, Fundamentals of Cosmic Physics, 5, 287
van Dishoeck, E. F., & Black, J. H. 1988, ApJ, 334, 771
Vigroux, L., Audouze, J., & Lequeux, J. 1976, A&A, 52, 1
Villanueva, V., Ibar, E., Hughes, T. M., et al. 2017, MNRAS, 470, 3775
Wall, W. F., Jaffe, D. T., Bash, F. N., et al. 1993, ApJ, 414, 98.
Wang, T., Elbaz, D., Alexander, D. M., et al. 2017, A&A, 601, A63
Wannier, P. G., & Sahai, R. 1987, ApJ, 319, 367
Watson, W. D. 1977, CNO Isotopes in Astrophysics, 105.
Wilson, R. W., Jefferts, K. B., & Penzias, A. A. 1970, The Astrophysical Journal, 161, L43
Wilson T. L., Rood R., 1994, ARA&A, 32, 191

Webb T. M., et al., 2003, ApJ, 582, 6
Watson W. D., Anicich V. G., Huntress W. T., 1976, ApJL, 205, L165
Young, J. S., & Sanders, D. B. 1986, ApJ, 302, 680.
Yang G., et al., 2018, MNRAS, 475, 1887
Yen, H.-W., Koch, P. M., Liu, H. B., et al. 2016, ApJ, 832, 204
Zhang, Z.-Y., Romano, D., Ivison, R. J., et al. 2018, Nature, 558, 260.

This paper has been typeset from a TEX/LATEX file prepared by the author.